Nanoscale

Accepted Manuscript

This article can be cited before page numbers have been issued, to do this please use: S. Patra, D. D. Yadav, G. Singh, J. Jyotirmayee, P. S. Samata, D. Pareek, A. S. Kudada, A. Mourya, D. Bhandary and P. Paik, *Nanoscale*, 2025, DOI: 10.1039/D5NR00281H.

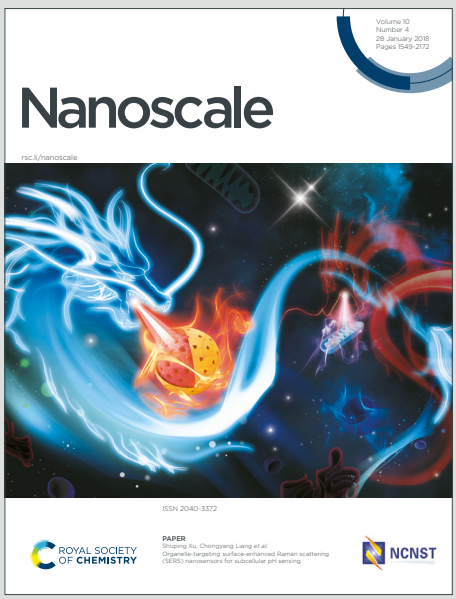

ROYAL SOCIETY OF CHEMISTRY

rsc.li/nanoscale

View Article Online
DOI: 10.1039/D5NR00281H

Full Research Paper

Self-assembled Amino acid-based copolymer Nanoparticles for Wound Healing and tissue regeneration: structure studied through Molecular Dynamic Simulation

Received 00th January 20xx,
Accepted 00th January 20xx

DOI: 10.1039/x0xx00000x

Sukanya Patra,[a] Desh Deepak Yadav,[a] Gurmeet Singh,[a] Jyotirmayee,[b] Prakriti Sundar Samanta,[a] Divya Pareek,[a] Aman Srikanta Kukada,[a] Anjali Ramsabad Mourya,[a] Debdip Bhandary [*c] and Pradip Paik[*a]

Amino acid-based block copolymer nanoparticles with cross-linkers have garnered growing interest in recent years. However, its' intricate synthesis and purification difficulties, along with stability concerns linked to intermicellar crosslinking, restrict their potential use in healthcare and therapeutic applications. In this line, the present work is aimed to design amphiphilic block copolymer nanoparticles of *N*-acryloyl glycine and *N*-acryloyl-(L-phenylalanine methyl ester), i.e., p(NAG-*co*-NAPA)$_{wc}$, without using a cross-linker via miniemulsion free radical polymerization. The self-assembled π-π stacking structural arrangement of copolymer at different temperatures has been confirmed through the molecular dynamics (MD) simulation, which corroborated the structural stability of copolymer nanoparticles at physiological temperature (37°C). The cell migration results of p(NAG-*co*-NAPA)$_{wc}$ nanoparticles are complementary to the CEMA assay and reveal their tissue regeneration properties. Further, the *in vivo* wound healing study demonstrated that within 13 days of post-treatment, the wound can be healed ~97%, whereas for the control, it is found to be only ~80%. Additionally, the RT-PCR results revealed that p(NAG-*co*-NAPA)$_{wc}$ nanoparticles possess anti-inflammatory and tissue regeneration properties by downregulating TNF-α and IL-1β; and upregulating PECAM-1 and VEGF-A, respectively. In conclusion, this p(NAG-*co*-NAPA)$_{wc}$ nanoparticles are paramount with an extensive clinical potential for the regeneration of acute wounds and can be used for other therapeutic applications.

Introduction

Amino acid-based random block copolymers have gained huge attention in biomedical applications due to their unique structures and molecular properties. Block copolymers can be self-assembled into various stable nano-objects based on the conditions applied.[1, 2] They can be conjugated with biomolecules, like drugs or genetic materials, or encapsulated through absorption/adsorption or chemical reactions on their surface or in the void space.[3, 4] Their biocompatibility and high bioavailability have received considerable attention over other properties.[5] The presence of hydrophilic/hydrophobic functional groups in polymer chains, it facilitates the smart attachment of other multiple blocks that subsequently helps in developing surface multi-functionality, high cross-linking, interlocking or branching structure, excellent solubility and symmetric effect. Further, the degradation of their secondary bonds causes pore formation, which may influence by varying the temperature, humidity, solvent and pH.[6]

Self-assembly, hydrothermal synthesis, phase separation, reversed atom transfer radical polymerization, and mini/macro emulsion radical polymerizations are often followed to synthesize polymer nanoparticles. Cross-linkers play a major role in minimizing premature disintegration and providing prolonged circulation time with controlled release of biomolecules.[7, 8] Polymeric nanoparticles with chemically bonded cross-linkers are more stable in high dilutions due to their complex interconnected network. However, they show poor response to any external stimuli and self-healing. Excessive use of cross-linkers makes the polymeric particle rigid and can cause severe toxicity to organs.[9] Further, cross-linkers are highly chemically active and tend to bind with the endothelial cells, body proteins, metal ions, enzymes and lipids.[10, 11] Major challenges lie with the cross-linkers that they can hinder the systematic cellular activities.[12] Due to all these limitations, a series of chemically synthesized covalently cross-linked nanoparticles is restricted for clinical trials.[13] On the other hand, non-covalently cross-linked polymeric nanoparticles are often favoured due to their dynamic evolution and ease of preparation.[14, 15] The stability of non-covalent cross-linked nanoparticles arises due to hydrogen bonds, dipole-dipole interactions, π-π stacking, coordination complexing and hydrophilic or hydrophobic interactions.[16] Double hydrophilic block copolymers of PEG-*b*-PNIPAM were synthesized following RAFT polymerization based on hydrogen bonds.[17] Similarly, phenylboronic acid-modified-PEG-*b*-P(Asp-co-AspPBA) was synthesized through the ROP approach to encapsulate insulin from the attack of external proteases, which was stabilized by hydrophobic interactions.[18] However, in both the cases the presence of PNIPAM limits their

[a] School of Biomedical Engineering, Indian Institute of Technology (BHU) Varanasi, Uttar Pradesh, India, 221 005Address here.
[b] School of Biotechnology, Institute of Science, Banaras Hindu University, Varanasi, Uttar Pradesh, India, 221005
[c] Department of Chemical Engineering and Technology, Indian Institute of Technology (BHU) Varanasi, Uttar Pradesh, India, 221 005

† Footnotes relating to the title and/or authors should appear here.

Supplementary Information available: [details of any supplementary information available should be included here]. See DOI: 10.1039/x0xx00000x

View Article Online DOI: 10.1039/D5NR00281H

extensive use in therapy. Compared to all other secondary interactions, π-π stacking provided more stability to the polymeric nanoparticles despite the presence of weak interactions. The π-π stacking is a spatial arrangement of phenyl rings that usually exists between two molecules deficient or abundant with electrons. The π-π stacking-based polymer micelles showed improved loading and delivery of hydrophobic drugs containing aromatic groups to tumors and a many-fold decrease in CMC.[19] The self-assembled polymeric nanoparticles supported by physical cross-linkers are often reversible and dynamic.[20] To enhance the noncovalent interactions and higher stability, self-assembled polymeric nanoparticles can be composed of both hydrophilic and hydrophobic units.[21] It can be noted that the non-covalently cross-linked self-assembled amino acid-based block copolymers is still to be explored with their therapeutic applications.

In the above line, the small size of the 'NAG' unit and the presence of a phenyl ring in the 'NAPA' unit motivated us to design a random di-block copolymer of *N*-acryloyl glycine (NAG) and *N*-acryloyl-(*L*-phenylalanine methyl ester) (NAPA), p(NAG-*co*-NAPA)$_{wc}$ via non-covalent cross-linking for biomedical applications. These self-assembly nature of the polymer chains could form the nanoparticles without using additional cross-linkers. Considering this, the self-assembled nature of the NAPA-NAG at different temperatures has been explored through the molecular dynamics (MD) simulation. The atomistically modelled p(NAG-*co*-NAPA)$_{wc}$ are allowed to reveal their internal properties using MD simulations. 500 dimer units of NAPA-NAG (as obtained from MALDI-ToF results) have been inserted randomly and solvated with water within an orthogonal periodic box and allowed to evolve for 100 ns. The effect of the temperature on the molecular morphology of dimers while forming self-assembled copolymer nanoparticles has been studied in detail. Through the MD simulation, we have further delved into the analysis of the structure of the agglomerates at different temperatures through analysis of the radial distribution functions between critical pairs. Further, how the interconnected network-like molecular morphology are formed that has also been predicted in presence of carboxylic and amide groups that could interact with water and help to stabilize the self-assembled polymeric nanostructures by electrostatic interactions. It can be noted that the exposure of these groups present on the surface of nanoparticles can also be ensured by surface potential. Hence, the MD simulation study has been employed to ensure the colloidal stability of such copolymer nanoparticles.

Additionally, NAG and NAPA monomers are highly soluble in organic solvents, and their copolymers are well known for their wide applications in healthcare as therapeutics.[22, 23] Therefore, the hemocompatibility and cytocompatibility of p(NAG-*co*-NAPA)$_{wc}$ nanoparticles have been studied against rat RBCs and L929 (mouse fibroblast), respectively, and their potential use in wound healing has been investigated through the scratch wound assay and CEMA assay. The present study further investigated the irritation and sensitization, levels of pro-inflammatory cytokines, and relative fold change in gene expressions of p(NAG-*co*-NAPA)$_{wc}$ nanoformulation in *in vivo* wound healing using Rats.

Results

Synthesis and Characterization of monomers (NAG and NAPA) and random block copolymers nanoparticles (p(NAG-*co*-NAPA)$_{wc}$).

The p(NAG-*co*-NAPA)$_{wc}$ was synthesized in two different steps. The first step was the synthesis of monomers (NAG and NAPA) (Scheme 1 (Step-1)) and followed by the synthesis of copolymer nanoparticles (Scheme 1 (Step-2)). The monomer synthesis was carried out using the Shorten Baumann reaction, where the amine group of amino acids reacts with acryloyl chloride in an alkaline medium to form an amide bond.[3, 23] The characteristic bands appeared in FTIR and NMR (^{1}H and ^{13}C) for both the monomers are shown in Figures S1-S3. For the synthesis of copolymer p(NAG-*co*-NAPA)$_{wc}$ nanoparticles, the free radical mini-emulsion polymerization method was followed as previously reported synthesis method (Scheme 1, step-3) with slight modification, i.e., avoiding the use of cross-linker (divinylbenzene).[3] In the p(NAG-*co*-NAPA)$_{wc}$ nanoparticles synthesis procedure, hexadecane (HD) was used as a co-stabilizer to increase the stability of the droplets formed in the emulsion process to prevent coagulation of the particles. Both the monomers were dispersed in the oil phase (toluene), and monomer droplets were formed. The radical initiator AIBN allows the initiation of the polymerization reaction at 65-75 °C within the oil/monomer droplet and at the interface of oil/monomer droplets and the aqueous phase. The oily core surrounded by a thin polymeric membrane was stabilized by cross-linking the monomer droplets with NAG, which can generate pores in the nanoparticles. The NAG to NAPA wt% ratio was maintained constant (i.e., 50:50) throughout the reaction process. SDS was used as an emulsifier. Nanoparticle synthesis without SDS causes a decrease in stability and forms aggregates during synthesis. The mechanism behind this copolymer synthesis is simple and straightforward. In brief, at first, AIBN initiates the reaction by attacking the hydrogen attached to the terminal sp^2-hybridized primary carbon of NAG and NAPA and forms radical ions of both monomers. Then these radicals propagate the chain and eventually the chain undergoes termination, where different growing chains meet 'head-to-head' by forming a π-bond (Scheme 2). The copolymer p(NAG-*co*-NAPA)$_{wc}$ formed is amphiphilicin nature, i.e., the carboxylic acid group (-COOH) in NAG and one phenyl ring present in NAPA provide hydrophilic and hydrophobic nature to the whole system, respectively. They form a self-assembled structure by moving phenyl rings towards the core of the micelle and carboxylic groups towards the outer side of the micelle. This arrangement of phenyl rings is facilitated by the electrostatic intramolecular π-π stacking among phenyl groups as reported by Hunter and Sanders in 1990.[24] Thus, this arrangement helps in generating a network-like copolymer without using any cross-linkers, and it promotes the stabilization of the NPs through the molecular packing.[25]

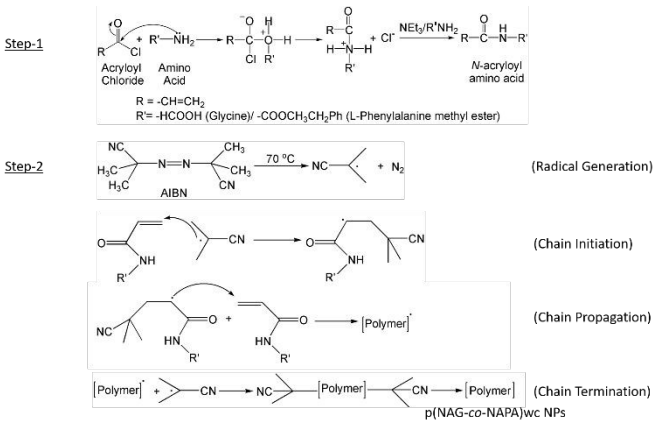

Scheme 1. Schematic represents the mechanism involved in the synthesis of NAG

View Article Online
DOI: 10.1039/D5NR00281H

(Step-1), NAPA (Step-1) and p(NAG-*co*-NAPA)$_{wc}$ nanoparticles (Step-2).

Further, chemical functionalities of p(NAG-*co*-NAPA)$_{wc}$ nanoparticles are confirmed through ^{1}H NMR, ^{13}C NMR and FTIR, and the molecular weight has been estimated through the MALDI-ToF. The position and number of hydrogen atoms present in p(NAG-*co*-NAPA)$_{wc}$ nanoparticles are confirmed through ^{1}H and ^{13}C NMR. The important bands are designated as follows: ^{1}H NMR (ppm): δ = 8.15 (1H, d, (secondary amine of NAG monomer)), 7.25 (1H, d, (secondary amine of NAPA monomer)), 7.15 (5H, m, aromatic H), 4.02 (3H, t, alkoxide), 7.05 (-C (=O) N) cis and 5.60 (-C (=O) N) trans, 3.96-2.37 (1H, m, (-CH2 adjacent to amide of NAG monomer)), 3.21-2.29 (1H, m, (-CH2 adjacent to amide of NAPA monomer)) and 2.51 (1H, dd, J= 11.3, 9.5) (Figure 1 (a)), ^{13}C NMR (ppm): disappearance of all the bands for monomers and only one band at δ ranging from 40.33 to 39.32 shows the splitting of 2° alkane (Figure S4) and FTIR (KBr), ν (in cm^{-1})= 3328 (secondary -NH, s), 3020 (aromatic –CH, s), 2925 and 2863 (alkane –CH, s), 1726 (ester C=O, s), 1649 (-NH-C=O, s), and 739 (aromatic –CH, b) (Figure 1 (b)). UV-Vis spectra confirm the formation of p(NAG-*co*-NAPA)$_{wc}$ nanoparticles with the absorption bands appearing at λ_{max} = 220 nm and 258 nm, corresponding to π-π* and n- π* transitions, respectively (Figure S5). The π-π* transition confirms the presence of the carbonyl group, while n- π* transition confirms the presence of double bonds in p(NAG-*co*-NAPA)$_{wc}$ nanoparticles. MALDI-ToF analysis confirms the molecular weight of the copolymers ranging from 377 Da to 493 Da, with an intense band at 400.02 Da, which depicts that possibly most of the fragments are nearly equal to the summation of the individual molecular mass of one NAG and one NAPA unit. Therefore, the highest intensity fragments consist of a dimer of NAG and NAPA. The first highest fragment is obtained at 406.31 (m/z), i.e., number average molecular weight ($\overline{M_n}$), and 400.02 (m/z), i.e., weight average molecular weight ($\overline{M_w}$), with a PDI of 0.99 representing uniform length of polymer chains. The difference between two adjacent peaks varies from 13 Da to 45 Da, which further confirms the formation of random p(NAG-*co*-NAPA)$_{wc}$ copolymer nanoparticles with a heterogeneous population in the system (Figure S6). Therefore, all these chemical functionality-based observations confirm the successful synthesis of p(NAG-*co*-NAPA)$_{wc}$ nanoparticles.

The thermal stability of p(NAG-*co*-NAPA)$_{wc}$ nanoparticles exhibits five steps of weight loss ranging from 130 °C to 356 °C (Figure 1 (c)). The thermal stability of the nanoparticles at physiological temperature (37 °C) is crucial for their use in therapeutic applications. The five steps weight loss (%): (I) 45-108 °C (3%), (II) 108-158 °C (3%), (III) 158-240 °C (13%), (IV) 240-310°C (21%) and (V) 310-390 °C (30%) are observed. Stage I is observed due to the loss of free moisture, and

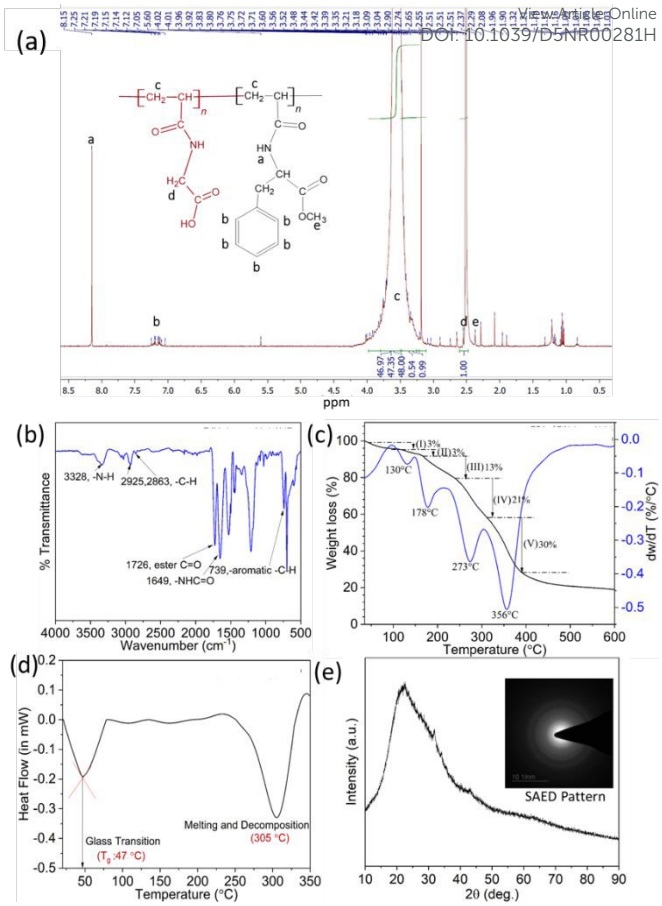

Figure 1. Physicochemical properties of p(NAG-*co*-NAPA)$_{wc}$ nanoparticles. (a) ^{1}H NMR spectra, (b) FTIR spectra, (c) TGA and DTGA thermograms, (d) DSC thermogram and (e) XRD pattern of p(NAG-*co*-NAPA)$_{wc}$ nanoparticles. Inset image of (e) is the SAED pattern for p(NAG-*co*-NAPA)$_{wc}$ nanoparticles.

stages II, III, IV, and V are observed due to the thermal degradation of polymer chains. It can be noted that beyond 390 °C, the leftover materials are the carbon residues only. The DTGA plot of p(NAG-*co*-NAPA)$_{wc}$ nanoparticles (Figure 1 (c)) provides an idea of degradation temperatures corresponding to each weight loss step. The maximum rates of degradation are found to be at 130 °C, 178 °C, 273 °C and 356 °C. Degradation at lower temperature is observed may be due to the presence of low molecular weight of p(NAG-*co*-NAPA)$_{wc}$ in nanoparticles. Furthermore, to evaluate the thermal phase transition, the DSC of p(NAG-*co*-NAPA)$_{wc}$ nanoparticles was conducted from RT to 350 °C (Figure 1 (d)). The glass transition temperature (T_g) is observed at 47 °C with an endothermic peak (endo down). An additional endothermic peak is observed at 305 °C due to the decomposition of p(NAG-*co*-NAPA)$_{wc}$ nanoparticles. From XRD, it is confirmed that the p(NAG-*co*-NAPA)$_{wc}$ nanoparticles are amorphous in nature, which matches well with the diffused ring of SAED patterns obtained from the HR-TEM image of p(NAG-*co*-NAPA)$_{wc}$ nanoparticles (Figure 1 (e) and inset image) represented in the subsequent section (Figure 2 (b)). The amorphous nature of p(NAG-*co*-NAPA)$_{wc}$ nanoparticles helps in improving the nanoparticle's apparent bioavailability.[26, 27]

Morphology and colloidal stability of p(NAG-*co*-NAPA)$_{wc}$ nanoparticles

The shape, size, and morphology of the p(NAG-*co*-NAPA)$_{wc}$ nanoparticles were investigated by using FESEM, HR-TEM and AFM analysis (Figure 2). The microscopic images (Figure 2 (a), (b) and (d)) revealed that p(NAG-*co*-NAPA)$_{wc}$ nanoparticles are spherical in nature with a diameter ranging from 120-400 nm. Figure 2 (e) represents the particle size distribution (120-200 nm) obtained from FESEM images. From HR-TEM images (Figure 2 (b)), the size was calculated to be 200-220 nm in diameter. From AFM, the size is calculated to be 200-300 nm in diameter. The variation in the sizes p(NAG-*co*-NAPA)$_{wc}$ nanoparticles obtained from different microscopy results is due to the different modes of the experimental procedure. However, the dark core-like structure as observed in Figure 2 (b) is due to the self-assembly nature of polymer chains of p(NAG-*co*-NAPA)$_{wc}$ nanoparticles, as shown in Scheme 2. This self-assembly occurs due to the presence of a hydrophilic carboxylic groups on the surface of the particle, which form a corona, and hydrophobic phenyl rings present inside the shell. The hydrophobic rings are arranged in T-shaped π stacking (Scheme 2). MD simulation study has been performed to confirm the self-assembly structure of p(NAG-*co*-NAPA)$_{wc}$ polymer chains in nanoparticles, which has been discussed in the subsequent section. Further, the colloidal stability of the p(NAG-*co*-NAPA)$_{wc}$ nanoparticles was checked by DLS in MilliQ at RT (Figure 2 (c)), and the hydrodynamic diameter is calculated from size distribution by intensity plot and the Z-Average is found to be 389 nm with 0.171 PDI. Further, volume distribution by intensity report and combined plot of intensity vs size and volume vs size are shown in Figure S7. The larger in size of p(NAG-*co*-NAPA)$_{wc}$ nanoparticles is observed due to the entrapment of water molecules in the copolymers' network and possible swelling of the nanoparticles.

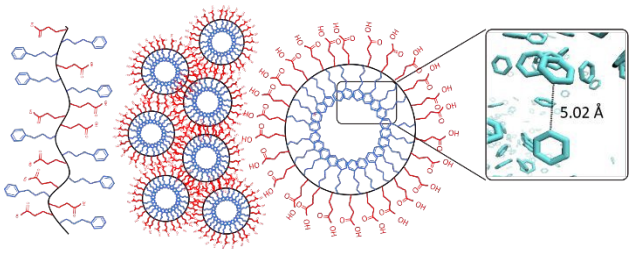

Scheme 2: Schematic representation of p(NAG-*co*-NAPA)$_{wc}$ nanoparticles forming self-assembled nanostructure via physical cross-linking induced by π-π stacking.

The zeta potential was calculated to be -50.94 mV, which comprises the colloidal stability of p(NAG-*co*-NAPA)$_{wc}$ nanoparticles (Figure 2 (f)). The optical properties of p(NAG-*co*-NAPA)$_{wc}$ nanoparticles were confirmed through the CD spectroscopy as mentioned in the experimental section with concentrations of 1000 to 125 μg mL^{-1} at 25 °C. In all concentrations, a distinct narrow CD band appeared at λ_{max} = (230 ± 5) nm (Figure 2 (g)) due to the presence of optically active NAPA monomer in the copolymer nanoparticles.[28] As reported earlier, with an increase in the concentration of nanoparticles (i.e., subsequently an increase in the concentration of NAPA monomer), the intensity of the CD spectra increases. From Figure 2 (g), it is evident that as the positive and negative bands are separated from each other comprising the formation of a self-assembled structure in the medium.[29] Further, by fixing the p(NAG-*co*-NAPA)$_{wc}$ nanoparticle's concentration at 125 μg mL^{-1}, CD spectra were recorded at three different temperatures (25 °C, 37 °C and 42 °C) (Figure 2 (h)). Similar CD spectra were obtained for each with λ_{max} = 218 nm, which comprises

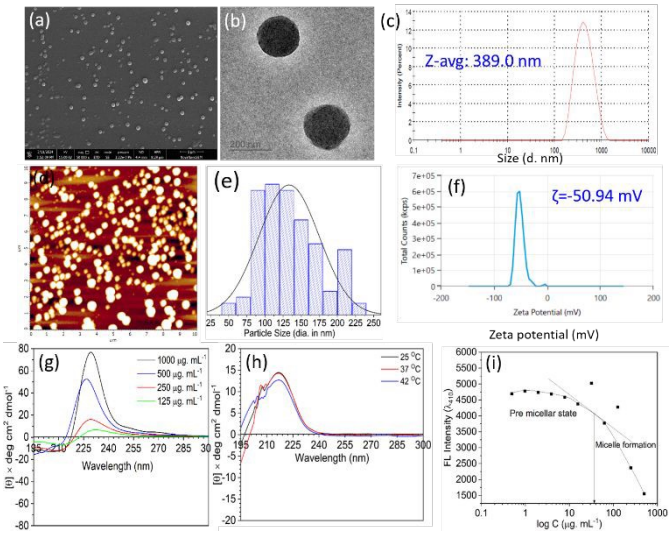

Figure 2. Size, shape, morphology and colloidal stability of p(NAG-*co*-NAPA)$_{wc}$ nanoparticles. (a) FESEM, (b) HRTEM image (scale bar: 200 nm), (c) DLS, (d) AFM, (e) particle size distribution obtained from Fig. 2 (a), (f) Zeta potential, (g) and (h) CD spectra of p(NAG-*co*-NAPA)$_{wc}$ nanoparticles at different concentrations and three different temperatures, respectively and (i) CMC of p(NAG-*co*-NAPA)$_{wc}$ nanoparticles.

the existence of secondary structure of the polymer chains in the copolymer nanoparticles. Using JASCO software, it is also identified that the copolymer consists of ~100% turn-type of secondary arrangements formed in the polymeric particles, with a few numbers of small loops consisting of hydrogen bonds (Figure S8). All these results also assist the formation of fibrils like of structural arrangement in the copolymer nanoparticle.[30] Subsequently, these secondary structures can help in understanding the interactions between nanoparticles and drug molecules, and further this can be helpful in designing a drug or vaccine with desired stability, shelf-life, and efficacy of treatment. The CMC is an important parameter in colloid chemistry, which denotes the minimum concentration needed to form a self-assembled structure of nanoparticles in the liquid medium. The magnitude of the CMC is closely related to the size of the nanoparticle and hydrophobic block present in the system. It can be noted that a block copolymer is biocompatible, and a precise ratio should be maintained between hydrophobic and hydrophilic units for its effective use in therapy.[31, 32] Herein, the CMC for the p(NAG-*co*-NAPA)$_{wc}$ nanoparticles were calculated to be 1.56 μg mL^{-1} (Figure 2 (i)). This low extent of CMC demonstrated that a good hydrophobic to hydrophilic ratio is maintained in the system with increase in the extent of π-π stacking due to the physical cross-linking. The MD simulation results also demonstrate that the benzene rings are present in close proximity with a distance of 5.02 Å (Scheme 2). This leads to the formation of aggregates of p(NAG-*co*-NAPA)$_{wc}$ nanoparticles in the particular medium or solvent. Furthermore, such systems with low CMC can tolerate the high degree of dilution, i.e., bloodstream dilution and makes the nanoparticles biologically and mechanically more stable. It can be further elucidated that the physical cross-linking can reform the nanoparticles even after disintegration of the self-assembly structure, which is known as self-healing of nanoparticles.[33, 34]

Molecular aggregation of p(NAG-*co*-NAPA)$_{wc}$ nanoparticles

View Article Online
DOI: 10.1039/D5NR00281H

Molecular dynamics simulations of atomistically modelled p(NAG-*co*-NAPA)$_{wc}$ molecules revealed the molecular organization in the presence of water. 500 dimers of NAG-*co*-NAPA were randomly inserted within an orthogonal periodic simulation box followed by solvation with water. The aqueous solution of NAPA-NAG, having a concentration of 0.2 g mL^{-1}, was allowed to evolve for 100 ns. The concentration of the dimer in the simulations is much higher compared to the concentration range used in the experiments (7.8-1000 µg mL^{-1}). To prepare the computational systems having concentration in this range, the number of solvent molecules in the simulation box would be very large (more than 200 times the present), and the computation would be extremely expensive and time-consuming.

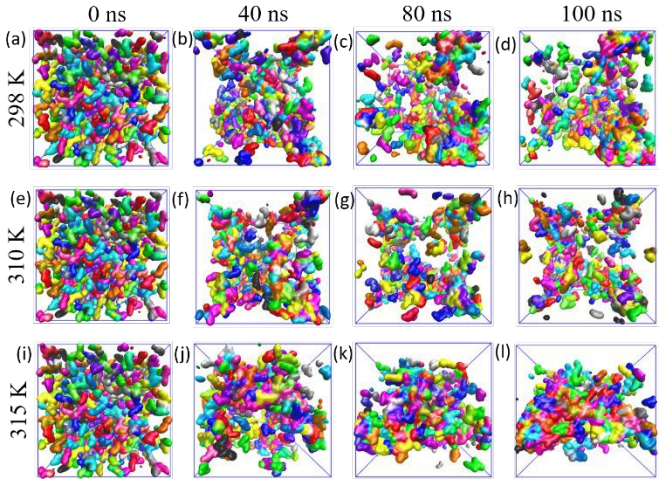

Figure 3. Show the structural evolution of NAPA-NAG at three different temperatures (298 K, 310 K and 315 K) at 0, 40, 80 and 100 ns. The dimers are represented as QuickSurf and other components of the solutions were omitted for visual clarity.

Figure 3 shows the evolution of dimer molecules in solution to reveal their organization and their structural properties at three different temperatures, such as 298 K, 310 K and 315 K. The initial configurations shown in Figure 3 (a, e, and i) indicated that the dimer molecules (different colours for different molecules) are randomly distributed in the water medium (not shown for clarity). From the snapshots in the top row of Figure 3, it is evident that the dimer molecules are forming interconnected aggregates (indicated by continuous surfaces with multiple colours) spreading over the whole simulation box. Additionally, Figures 3(c) and 3(d) indicate that the interconnected aggregates evolved their structure with time. However, the interconnected aggregates are building up the walls of the porous structure as observed in experiments. From Figure 3(e-f), it is revealed that the NAG-co-NAPA dimer molecules are also forming interconnected structures at 25 °C (298 K), which further manifests the porous structure of the nanoparticles obtained in the experiments. As the temperature rises to 37 °C (310 K), the number of interconnected fragments decreases (Figure 3 (g-h); hence, the porosity in the structure decreases. However, this extent of change is negligible. At 42 °C (315 K) at 40 ns, a distinct agglomeration is observed (Figure 3 (j) compared to the 25 °C and 37 °C (Figure 3(b) and 3(f)), respectively). However, at 80 ns, a deviation is observed with respect to the previous two cases. This phenomenon is observed as a larger number of agglomerated units were present (Figure 3(k)) which are surrounded by water molecules. This would lead to the formation of structure with less porosity. However, till 100 ns (Figure 3(l)) the structure remained alike. This revealed that there is an impact of temperature on the molecular morphology of dimers while forming nanoparticles. Further, the interconnected network-like molecular morphology of nanoparticles also indicated that the hydrophilic groups such as carboxylic and amide are interacting with water molecules strongly and prefer to be exposed to water. These molecular arrangements help in stabilizing the structure of the nanoparticles. The presence of these groups at the surface of nanoparticles justifies the negative zeta potential (Figure 2 (f)) that ensures the colloidal stability of the designed nanoparticles in aqueous medium. Additionally, to establish a better correlation, the aggregation behaviour of hydrophobic phenyl groups presents in NAPA units and hydrophilic carboxyl groups present in NAG units after 0, 40 and 80 ns of simulation run in the three concerned temperatures as shown in Figures S10 and S11.

Structural Properties of p(NAG-*co*-NAPA)$_{wc}$ Molecular Assembly

We further delved into the analysis of the structures of the agglomerates at different temperatures through analysis of the radial distribution functions between critical pairs of atoms. In Figure 4 (a-c), the radial distribution function of pairs, such as water-carboxylic, water-phenyl, and water-amine groups are shown at different temperatures. The pair correlation between the carboxyl groups and the water molecules is strong, as indicated by the appearance of the sharp repetitive peaks at regular intervals. However, the local density of the water molecules has not reached to the overall density of the system, comprising the formation of an agglomerated structure (Figure 3). Another interesting aspect to note here is the drop in the peak intensity with temperature. This observation suggested that the solvation shells gradually become less populated as the temperature rises. The pair correlation between the water and phenyl groups did not pose a sharp peak (Figure 4 (b)), indicating the presence of a structured water layer surrounding the phenyl rings due to the electronic cloud of the phenyl rings. The pair correlations gradually increase towards unity, suggesting the formation of an overall agglomerated structure. In the case of this pair, the number of water molecules present around the phenyl rings also decreased with an increase in the temperature of the system. The amide/amine nitrogen atoms, however, showed a stronger affinity with water molecules compared to the phenyl groups, as indicated by the appearance of a sharp peak (Figure 4 (c)). It is also revealed that the amine groups hold the water molecules at ~2.8 Å, which allows the formation of hydrogen bonds with the nitrogen atoms. In this case, the peak height is decreased slightly with an increase in temperature. Further, the coordination numbers for 310 K to 315 K are found to be higher in value compared to the temperature range of 298 to 310 K (inset Figure 4 (c)). The interplay between hydrophilic and hydrophobic groups has played a key role in the aggregation of copolymers. More specifically, the hydrophobic phenyl groups played a crucial role in agglomeration due to possible π-π stacking. Further, we have calculated the RDF between carbon atoms at the 1 and 4 positions of different phenyl rings, denoted as Ph11, Ph14, and Ph44 (Figure 4 (d)). In this Figure, the comparisons of RDFs between different pairs are shown at different temperatures. The 4-4 pairs correlation showed a stronger split of peaks at lower distances, whereas the other pairs exhibited weaker peaks at higher distances. This indicated that the 4-4 interactions are quite stronger and thus played a dominating role in agglomerating the dimers. However, the structure is amorphous in nature, as indicated by the absence of any sharp peak. This dominance for Ph44

View Article Online
DOI: 10.1039/D5NR00281H

could be due to its readily accessible position, along with the presence of a bulky group with Ph11. Hence, to avoid steric hindrances, close associations of 4-4 pairs are favoured across all three temperatures, demonstrating a T-shaped π-π stacking. Furthermore, the histograms of angle distribution at three different

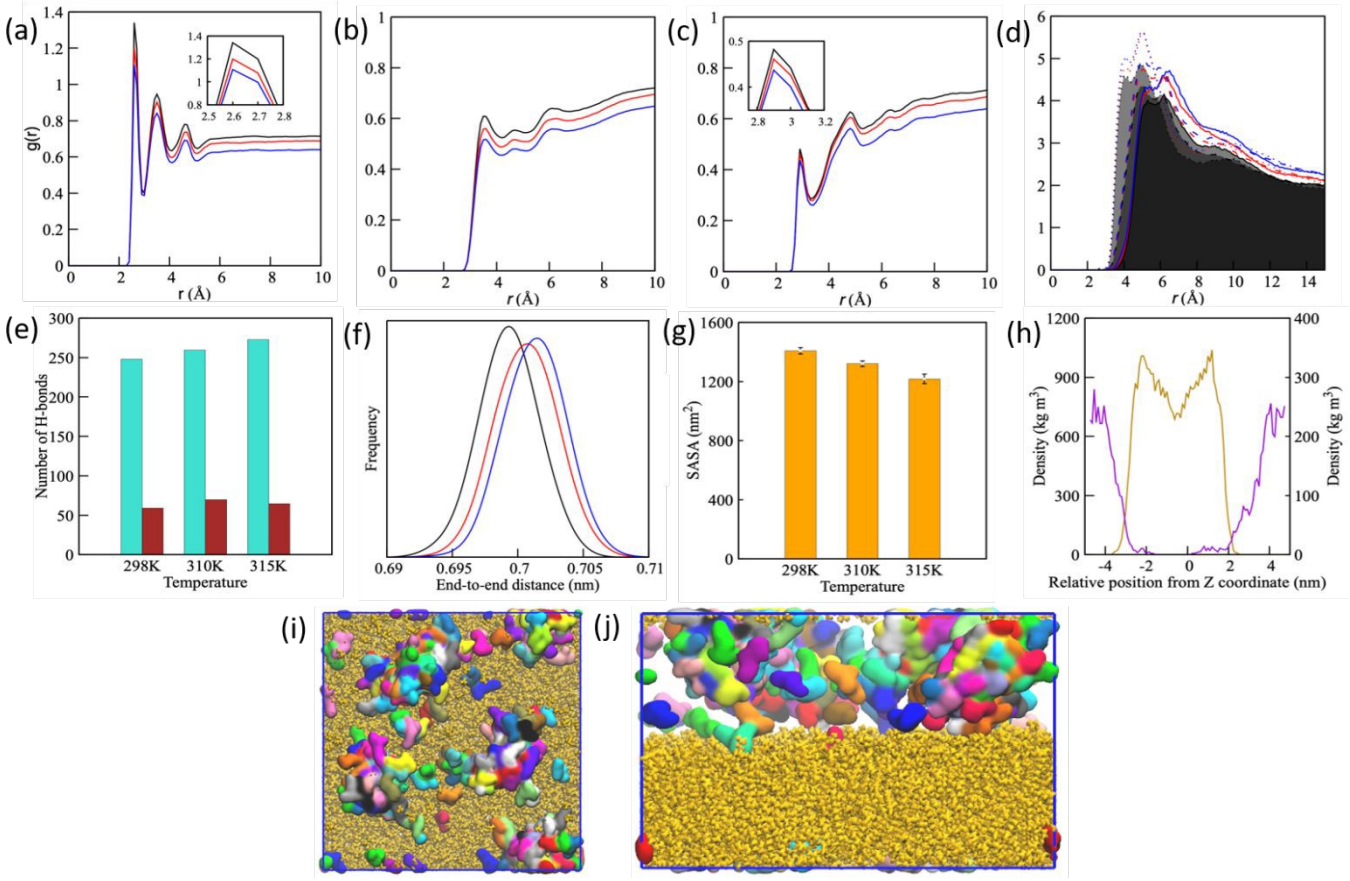

Figure 4. The radial distribution function between oxygen atoms in water molecules and (a) the carboxylic groups, (b) phenyl groups, (c) nitrogen atoms in dimers at different temperatures. The black, red and blue lines of figures represented the temperatures, 298, 310 and 315 K, respectively. (d) radial distribution functions between phenyl carbon atoms at 1 and 4 positions at different temperatures, respectively, (e) Number of intramolecular hydrogen bonds between –COO and –NH atoms with the total number of hydrogen bonds between dimer units at different temperatures, (f) distribution of end-to-end distance of the dimers at different temperatures, (g) Change in SASA of dimers matrix in aqueous solution at different temperatures with the evolution time, (h) density distribution of dimer and POPC membrane along the direction perpendicular to the membrane surface, and (i-j) side and top views of agglomerates of dimers in water on POPC membrane at 310 K, respectively.

temperatures are provided in Figure S12. On the other hand, the 1-1-pair correlation exhibited a broader split peak at a longer distance. Whereas, interestingly the 1-4 pairs showed a crossover of the RDF of two individual pairs. As the temperature of the system increases, all the RDF peak height increased as well as broadened. This indicates that the amorphous nature of the agglomerates increases with increase in temperature.

Further, to elucidate the behaviour of dimers in the aqueous system, the number of hydrogen bonds plays a pivotal role in aggregation between the dimers and water molecules, which was calculated at all temperatures. The average number of hydrogen bonds formed between dimers as shown in Figure 4 (e). Additionally, the intermolecular hydrogen bonds are formed predominantly. However, the total number of hydrogen bonds formed is approximately five times more than that of the intramolecular hydrogen bonds formed between the carboxylic acid groups and amine groups. The total number of hydrogen bonds increased with the increase in temperature, while the extent of intramolecular binding decreased.

At lower temperatures, due to the presence of a large number of intramolecular hydrogen bonds, a less interconnected hydrogen-bonding network formed that leads to the inclusion of more water molecules in the agglomerates. However, with increase in temperature, the molecules assembled into a larger network through the formation of hydrogen bonds, allowing the molecules to agglomerate tightly in an elongated manner. Additionally, the number of hydrogen bonds formed between dimers and water molecules are shown in Figure S13 (a) at three temperatures, which also further demonstrates that with increase in temperature, there is a sharp decrease in the number of hydrogen bonds. This decrease in the extent of hydrogen bonds matches well with the number of contact results as shown in Figure S13 (b). The end-to-end distribution of the dimers also quantifies the elongation of the molecules, as shown in Figure 4 (f). As the temperature increases, the end-to-end distribution of peaks is shifted towards the right, indicating the formation of a more

elongated conformation of the molecules in the agglomerate. Hydrophilicity of the agglomerated structure is a key parameter in utilizing it for therapeutic applications. Thus, we have calculated the solvent accessible surface area (*SASA*) to quantify it (Figure 4 (g)). It can be seen that with an increase in temperature, *SASA* decreases, which supports the hydrophobic nature of the agglomerates. A lower *SASA* value at 315 K hints towards the formation of larger globular

aggregates. However, a higher *SASA* is available at the physiological temperature (310 K). These findings suggest that higher aggregation occurred at higher temperature and subsequently it helps in stabilizing the nanoparticles. Additionally, the biocompatibility of dimers was assessed through the interactions with the POPC bilayer membrane at 310 K. The density distribution of dimers shown in Figure 4 (h) was calculated around the z-axis of the membrane, showing that dimer aggregates (Figure 4 (i)) have formed bonds to the membrane within 100 ns. Further, the dimers formed a close association with the bilayer surface of the membrane as shown in Figure 4 (j).

Biocompatibility, Hemocompatibility, Proliferative and migratory behavior of p(NAG-*co*-NAPA)$_{wc}$ nanoparticles through *in vitro* study.

Biocompatibility and hemocompatibility are the major parameters that need to be studied for any biomedical application of copolymer nanoparticles. The fibroblast cells are abundantly present in mammals and we have selected L929 cells to check the biocompatibility of the developed p(NAG-*co*-NAPA)$_{wc}$ nanoparticles. It is noticed that L929 cells treated with p(NAG-*co*-NAPA)$_{wc}$ nanoparticles demonstrated concentration-dependent proliferative behaviour and are cytocompatible in nature. Additionally, as the concentration of p(NAG-*co*-NAPA)$_{wc}$ nanoparticles increases, the cell viability (%) steadily increases. However, from 500 to 1000 µg mL^{-1}, cell viability (%) slowly decreases. This decrease in cell viability (%) is obtained due to the high contact inhibition experienced by cells in the respective confined space for a longer period of time (24h). It is worth mentioning that the concentrations of p(NAG-*co*-NAPA)$_{wc}$ nanoparticles taken 7.8125, 15.625, 31.25, 62.5 and 125 µg mL^{-1} and the cell viability (%) are observed to be 137.1±2.3, 122.9±2.5, 119.2±1.9, 119.9±1.2 and 119.3±1.4, respectively (Figure 5 (a)). These results clearly suggest that the designed p(NAG-*co*-NAPA)$_{wc}$ nanoparticles are biocompatible and can promote the proliferation of L929 cells. Further, hemocompatibility is also a crucial parameter for nanobiomaterials for their use in therapeutic applications, as the nanoparticles during systemic circulation can cause toxic effects and limit the therapeutic benefits.[36] The copolymer should have hemolysis below 5% to avoid any toxic effect. Thus, the haemolytic activities of p(NAG-*co*-NAPA)$_{wc}$ nanoparticles were studied in both dose and time-dependent manner over a range of 500 to 7.8125 µg mL^{-1} concentrations at 2 and 8 h. Herein, distilled water was considered as a positive control and pure RBC suspension was considered as a negative control. Although a varied degree of hemolysis (%) was observed at the concerned time for all the concentrations taken in this study, the exhibited hemolysis calculated to be below 5% (Figure 5 (b)). At 500 µg mL^{-1}, hemolysis values are observed to be 8.0±1.1 % and 10.1±1.5 % for 2 h and 8 h, respectively (Figure 5 (b)). In conclusion, the p(NAG-*co*-NAPA)$_{wc}$ nanoparticles can be considered as a safe biomaterial, which can be used up to 250 µg mL^{-1} for various therapeutic applications.

Skin fibroblast cells migration is an important aspect of regenerative medicine and wound healing processes.[37] As the cell proliferative behaviour of p(NAG-*co*-NAPA)$_{wc}$ nanoparticles was studied from

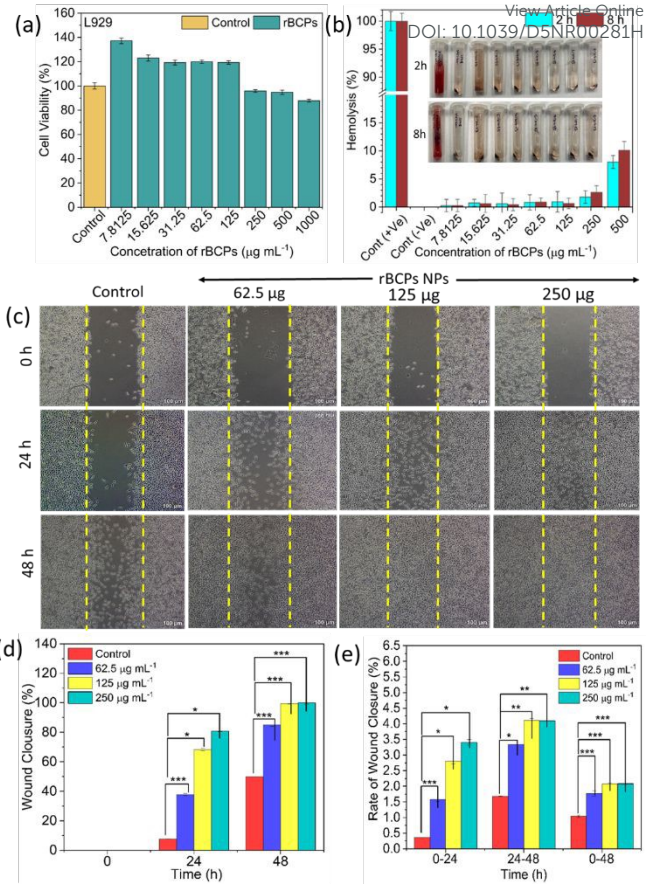

Figure 5. Biocompatibility, hemocompatibility and proliferation nature of p(NAG-*co*-NAPA)$_{wc}$ nanoparticles. (a) cell viability (%), (b) hemolysis (%) of p(NAG-*co*-NAPA)$_{wc}$ nanoparticles at different concentrations against L929 cells and rat erythrocytes, respectively. The inset image of figure 5 (b) represents the tubes micro-centrifuge tubes showing hemolysis at 2h and 8h. MTT of p(NAG-*co*-NAPA)$_{wc}$ nanoparticles shows no significant difference for both L929 and hemolysis (%) of nanoparticles are non-significant with respect to the control (-ve) and significant (*) with respect to the control (+ve) for 2 and 8 h, respectively. Hemolysis (%) for 500 µg mL^{-1} is significant (**) with respect to the control (-ve) at 8 h. Fig. (c) Represents the microscopic images of the wound scratch assay of p(NAG-*co*-NAPA)$_{wc}$ at 0, 24 and 48 h taken at 10X magnification with a scale bar of 100 µm, (d) and (e) Wound closure (%) and Rate of wound closure (%) of L929. rBCPs represents p(NAG-*co*-NAPA)$_{wc}$ nanoparticles. Data are given as mean ±SD (n=3) (*p ≤ 0.05, **p ≤ 0.05-0.01, ***p ≤ 0.05-0.001 and ns: non-significant).

the cell viability assay. Further, the pro-migratory effect of p(NAG-*co*-NAPA)$_{wc}$ nanoparticles was checked using an *in vitro* wound scratch assay for a period of 0 to 48 h at three different concentrations (62.5 to 250 µg mL^{-1}). At three different time points, optical microscopic images were acquired as shown in Figure 5 (c). It is observed that p(NAG-*co*-NAPA)$_{wc}$ nanoparticles can efficiently cover the wounds in L929 cells.

Furthermore, to quantify the wound closure efficiency (%) and wound closure rate (%), Fiji ImageJ software was used.[38] After 24 h of incubation of cells with p(NAG-*co*-NAPA)$_{wc}$ nanoparticles, 37.84±0.06%, 68.32±0.8% and 80.76±0.0009% of scratched area are filled for 62.5, 125 and 250 µg mL^{-1}, respectively. Whereas, for the control, 7.55±0.06% of the scratch is covered (Figure 5 (d)). After 48 h of incubation, 84.97±0.9%, 99.56±0.3%, and 99.94±0.007% of the scratched area are covered for 62.5, 125, and 250 µg mL^{-1}, respectively. Whereas for the control, only 49.86±0.2% of the scratch is covered (Figure 5 (d)). Further, it is noticed that during the initial 24 h, over all three concentrations, wound closure rate (%) is quite faster as compared to the next 24h. In case of wound closure rate (%), a similar trend is observed (Figure 5 (e)). From 0-24 h and 24-48 h, the wound closure rate is quite faster as compared to 0-48 h. These variations in results are observed due to the contact inhibition and

View Article Online
DOI: 10.1039/D5NR00281H

confined space available for the cells to proliferate and migrate. The results obtained from the wound scratch assay demonstrated that p(NAG-*co*-NAPA)$_{wc}$ nanoparticles can fill the scratched area by ~10 times more efficiently compared to the control. From both wound closure (%) and rate of wound closure (%) results, it is clearly evident that p(NAG-*co*-NAPA)$_{wc}$ nanoparticles show dose-dependent proliferative and migratory efficiency. Furthermore, it is evident that even at a very low concentration of 62.5 µg mL^{-1} the p(NAG-*co*-NAPA)$_{wc}$ nanoparticles can accelerate the wound healing efficiency.

Dose and time-dependent angiogenic nature of p(NAG-*co*-NAPA)$_{wc}$ nanoparticles

Angiogenesis plays an important role in the field of wound healing and regenerative medicine. It is a process where the new blood vessels emerge and/or proliferate from existing blood vessels.[39] As the results obtained from the cell viability study (Figure 5 (a)) and wound scratch assay (Figure 5 (c-e)) against L929 cells demonstrated that p(NAG-*co*-NAPA)$_{wc}$ nanoparticles are proliferative in nature. Further chicken embryo membrane assay (CEMA assay) was performed to establish the angiogenic or vascular sprouting nature of p(NAG-*co*-NAPA)$_{wc}$ nanoparticles. For this, three different doses (62.5, 125 and 250 µg) of p(NAG-*co*-NAPA)$_{wc}$ nanoparticles were incubated separately with chick embryos. It is revealed that the presence of p(NAG-*co*-NAPA)$_{wc}$ nanoparticles causes an increase in the thickness of blood vessels and length (Figure 6 (a)).

Further to quantify the angiogenic properties, Explant area, Vessel area, Junction density and Mean-E-lacunarity were calculated as mentioned in the experimental section. The explant area means the overall region where blood vessels are developed. It is observed that compared to the control, at 125 and 250 µg doses, very little explant area has been increased. While for the 62.5 µg dose, ~80% increase is observed at 8 h (Figure 6 (b)). A similar result is observed in the case of the Vessel area (%). Vessel area means the total surface area of blood vessels occupied in an explant area. Herein, at a lower dose, the vessel area is increased up to 180% (at 8 h), while for a higher dose, it is increased up to 140% (Figure 6 (c)). In case of junction density, a decrease in percentage is observed at lower dose, while for a higher dose, a slight increase in Junction densities is observed (Figure 6 (d)). Further, Mean-E-lacunarity (%) was also quantified, which suggests the empty spaces available after the incubation with the nanoparticles. In the case of a 62.5 µg dose, the Mean-E-lacunarity (%) is decreased to 69%, whereas for the control, it is found to be 88% at 8 h. However, in application of higher doses such as 125 and 250 µg, no such variation in Mean-E-lacunarity (%) is observed (Figure 6 (e)). However, based on time points from 0 to 8 h, in all considered parameters 62.5 µg dose, it is also showing better angiogenic in nature as compared to the other doses. Thus, the results obtained from CEMA assay clearly depicted that p(NAG-*co*-NAPA)$_{wc}$ nanoparticles are showing branching angiogenesis rather than sprouting of new blood vessels in dose and time-dependent manner, where the length and thickness of the developed blood vessels are found to be increased up to 8 h of incubation. These results are matching well with the previously obtained cell-based studies (Figure 5) and suggest that p(NAG-*co*-NAPA)$_{wc}$ nanoparticles are angiogenic in nature at lower doses in a time-dependent manner and are effective for regenerative purposes.

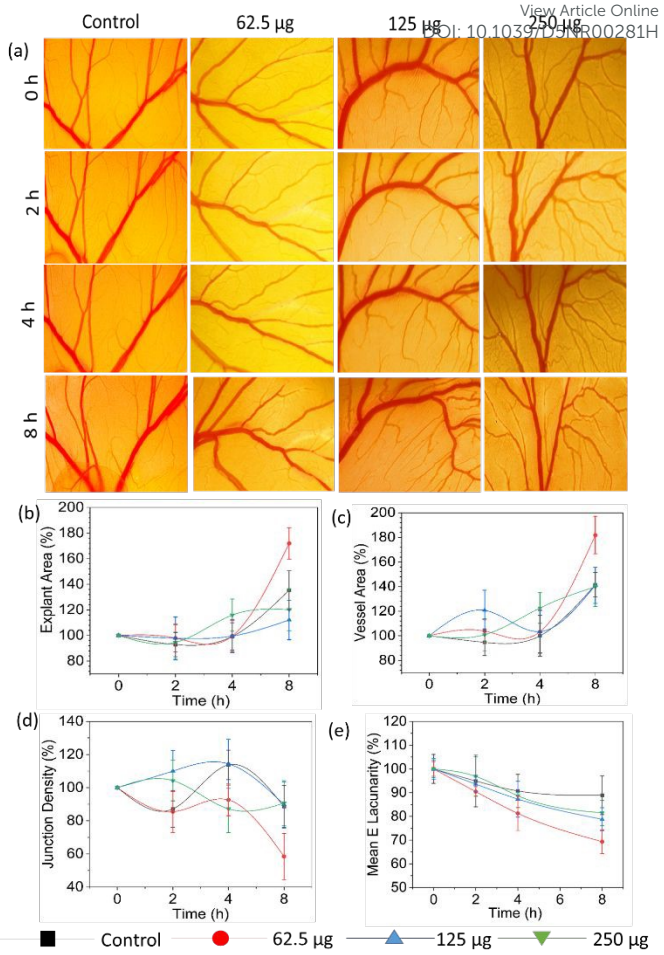

Figure. 6 Angiogenic effect of p(NAG-*co*-NAPA)$_{wc}$ nanoparticles. (a) *In ovo* CEMA assay in the presence of p(NAG-*co*-NAPA)$_{wc}$ nanoparticles support the branching angiogenesis in dose dependent manner. (b)-(e) represents several % changes in angiogenic parameters in percentage like Explant area, Vessel Area, Junction Density and Mean-E-Lacunarity, respectively in time and dose dependent manner.

In vivo wound healing efficacy of p(NAG-*co*-NAPA)$_{wc}$ nanoformulation

To check the *in vivo* wound healing efficiency of the prepared p(NAG-*co*-NAPA)$_{wc}$ nanoparticles, a nanoformulation was developed. This nanoformulation was prepared by triturating the p(NAG-*co*-NAPA)$_{wc}$ nanoparticle with an oleaginous base (see Table S2) as mentioned in the method section. To avoid any kind of incongruities, it was examined for phase homogeneity, discolouration and aggregations. It seems to be smooth, consistent and devoid of any aggregation by observing under white light and touching (Table S3). As the target application is wound healing, therefore initially a skin irritation study was performed with p(NAG-*co*-NAPA)$_{wc}$ nanoformulation, oleaginous base, –ve control with no treatment, and +ve control with application of 1% formalin. For the reference, the irritation nature of 1% formalin was also tested with the *in ovo* model up to 24 h, and the images are shown in Figure S15. After 48 h of treatment, it is observed that, other than the +ve control group, no other groups exhibited skin irritation (Figure 7 (b1), (b3), and (b4)). In the +ve control group, a substantial irritation at the site of application is clearly observed (Figure 7 (b2), black dashed circle). Further, the histology images were acquired from respective rat skin (Figure 7 (c-b4) and demonstrated that in +ve control group, damage

View Article Online
DOI: 10.1039/D5NR00281H

areas are persisting in epidermis layer of skin (Figure 7 (c2), black dashed circle), whereas

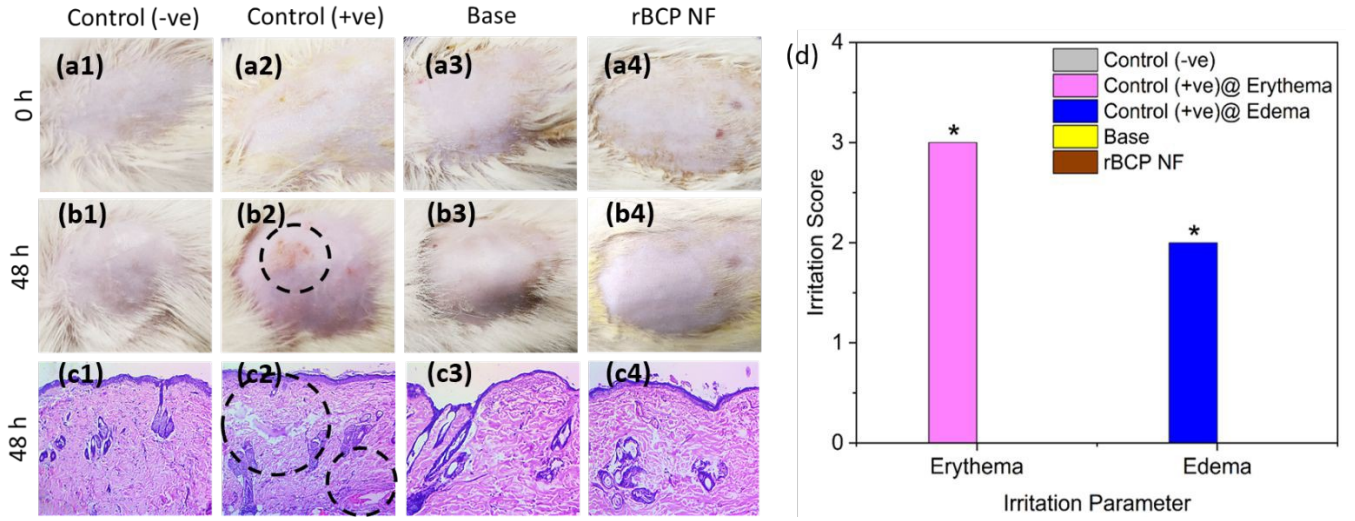

Figure 7. *In vivo* skin irritation study. (a1-a4) Camera photographs of skin irritation study captured at 0 h (before treatment) and (b1-b4) at 48 h (after treatment), (c1-c4) histology images of H&E staining of tissue samples collected from b1-b4 rat skin at 20X magnification, and (d) calculation of irritation score based on occurrence of erythema and edema after 48 h of treatment. The scale or erythema and edema are given in Table S4. rBCP NF represents p(NAG-*co*-NAPA)$_{wc}$ nanoparticles based nanoformulation. Data are given as mean ± SD (n=3) (*p ≤ 0.05, **p ≤ 0.05-0.01, ***p ≤ 0.05-0.001 and ns: non-significant).

in all other three cases, layers of skin tissue are highly intact with no damage. Furthermore, for the sensitivity study, the development of erythema and edema is observed and certain values are assigned to each rat based on the irritation score (Table S4). It is observed that only the +ve control group has developed erythema (value = 3) and edema (value = 2) on the skin (Figure 7 (d)). The PDII score for the +ve control group and other groups is found to be 2 and 0.25, respectively. Which signifies that the p(NAG-co-NAPA)wc nanoformulation is non-irritant and non-sensitive to the skin up to 48 h. Furthermore, this formulation ensures its use in effective wound healing.

The *in vivo* wound healing experiments were performed on Wistar rats as mentioned in the methods section. For clear understanding, a timeline is provided in Figure 8 (a), which represents the procedure from day 0th (wound creation) to 15th day of post treatment. The impact of p(NAG-*co*-NAPA)$_{wc}$ nanoformulation was assessed and compared with the control and base (Figure 8). It can be noted that wound healing is a normal phenomenon of body homeostasis with time. However, from Figure 8 (b1-b15), it is evident that the wound healing progress is swift in p(NAG-*co*-NAPA)$_{wc}$ nanoformulation followed by base. However, for the control group, it is delayed (Figure 8 (c)). In the control group, complete wound closure is not achieved even after 13 days of post-treatment, and subsequently the wound closure rate is also increased for p(NAG-*co*-NAPA)$_{wc}$ nanoformulation at least 2-3 days earlier as compared to the control group. Moreover, the relative wound area (%) was calculated and shown in Figure 8 (c). The corresponding wound areas (%) are found to be 94.96±2.04, 86.65±2.03, and 80.66±1.94 for control; 51.30±1.63, 54.98±2.20, and 30.55±1.36 for base, and 83.33±4.20, 54.00±3.96, and 32.21±3.16 for p(NAG-*co*-NAPA)$_{wc}$ nanoformulation on 4th, 7th and 10th day of post-treatment, respectively. Although on the 7th and 10th day of treatment, both the base and p(NAG-*co*-NAPA)$_{wc}$ nanoformulation are exhibiting similar healed areas (%), however, on the 13th day, it decreases from 12.06±4.05 % for base to 3.71±3.26 % for p(NAG-*co*-NAPA)$_{wc}$ nanoformulation group. Particularly, on day 7th, it is clearly visible from the wounded image of the base (Figure 8 (b8)) that some redness is observed on the skin. This redness may appear due to the inflammation that occurred in the presence of the base component only.

To confirm this phenomenon, further inflammatory markers were checked and they supported our results, which are discussed in the subsequent sections. Additionally, it can be noted from the wounded images (Figure 8 (b1-b15)) that from the 4th day in all groups, wound scabs developed and subsequently prevented the passage of blood and any fluids.[40] Although this early inflammatory healing stage is observed in all groups, progress is predominantly observed more in the p(NAG-*co*-NAPA)$_{wc}$ nanoformulation group as shown in Figure 8 (b12). As anticipated, on the 7th day of post-treatment, the production of granulation tissue in the p(NAG-*co*-NAPA)$_{wc}$ nanoformulation-treated groups is significantly higher in the p(NAG-*co*-NAPA)$_{wc}$ nanoformulation group than control groups, and by the 13th day of post-treatment the wounds in the p(NAG-*co*-NAPA)$_{wc}$ nanoformulation group are completely surrounded and covered by fully developed skin layers. In contrast, a significant wound area is still remained unhealed in the control group. To support all these

View Article Online
DOI: 10.1039/D5NR00281H

Full Research Paper

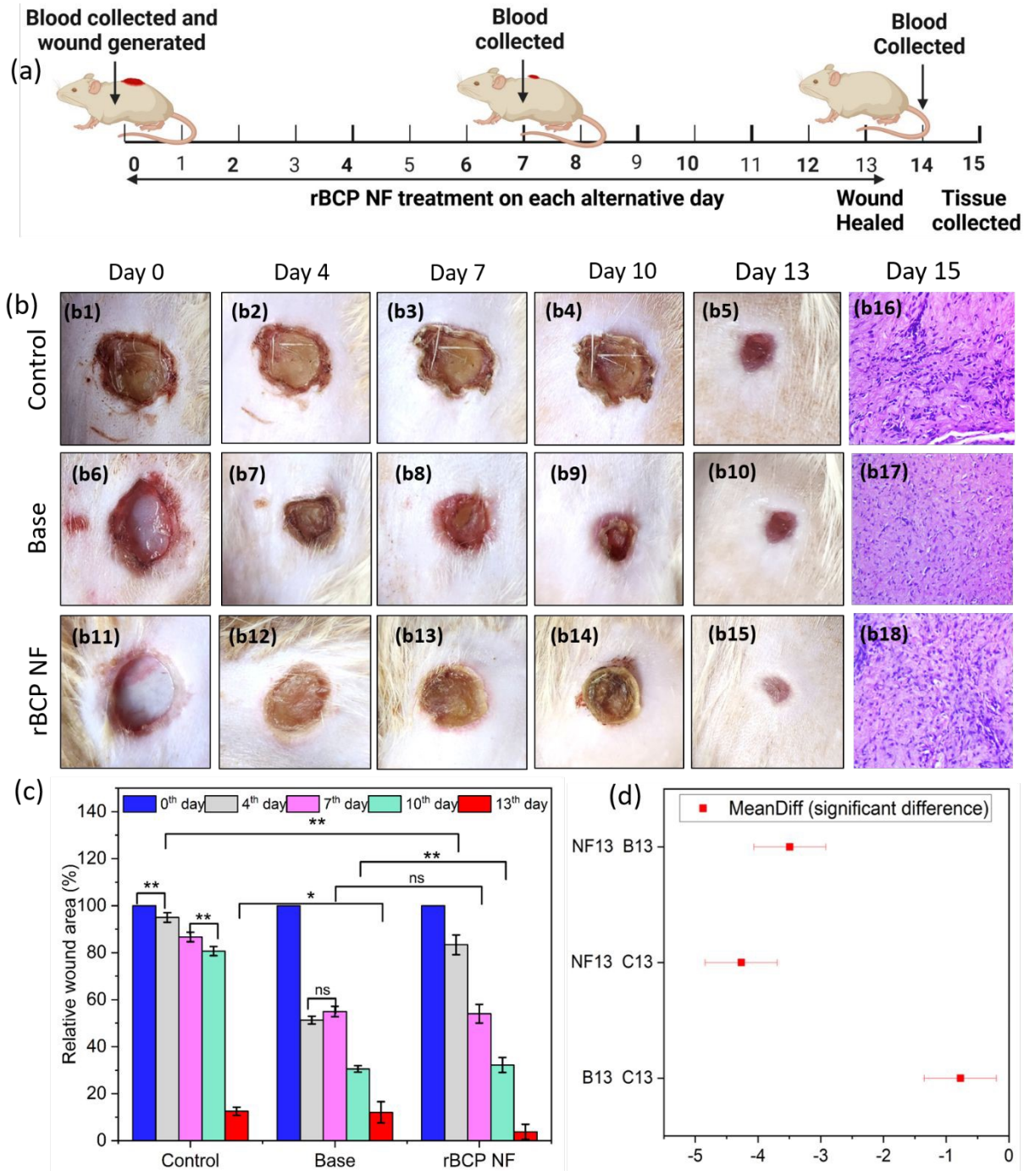

Figure 8. Represents *in vivo* wound healing results. (a) Timeline of *in vivo* animal experiment followed in this work, (b) Optical microscopy images of wounds in three different groups (Control (b1-b5), Base (b6-b10) and rBCP NF (b11-b15) acquired in high resolution camera on 0^{th}, 4^{th}, 7^{th}, 10^{th} and 13^{th} days and (b16-b18) histology images of H&E staining of healed tissue on 15^{th} day of post treatment of control, base and rBCP NF, respectively, acquired at 20X magnification, (c) Relative wound area (%) at five different days (0^{th}, 4^{th}, 7^{th}, 10^{th} and 13^{th}) remaining to heal, and (d) Significant difference of mean wound area on 13^{th} day using the Turkey test to compare the mean in between three different groups. In figure 7 (d), C: Control group, B: Base group and NF: rBCP nanoformulation. Other than represented statistical significance, all other combinations are significant with $P \leq 0.001$. rBCP NF represents p(NAG-*co*-NAPA)$_{wc}$ nanoparticles based nanoformulation. Data are given as mean ±SD (n=3) (*P ≤ 0.05, **P ≤ 0.05-0.01, ***P ≤ 0.05-0.001 and ns: non-significant).

View Article Online
DOI: 10.1039/D5NR00281H

Full Research Paper

findings, histology study was performed for the tissue samples collected on the 15th day of post treatment (Figure 8 (b16-b18)). From images, it is clearly evident that in the control group the clumped fibroblasts are generated. On the other hand, in the base and p(NAG-*co*-NAPA)$_{wc}$ nanoformulation groups, well-defined dispersed fibroblasts are present. Further, among the base and p(NAG-*co*-NAPA)$_{wc}$ nanoformulation groups, more fibroblasts are present in the wounded area of the p(NAG-*co*-NAPA)$_{wc}$ nanoformulation group. This increased number of fibroblast cells suggested that on the day 15th of post-treatment a well-defined skin layer is formed and the wound is completely covered (Figure 8 (b18)). Furthermore, a significant difference in mean wound area on the day 13th using the Turkey test is shown in Figure 8 (d) to compare the means among all the groups. Thus, the developed p(NAG-*co*-NAPA)$_{wc}$ nanoformulation can enhance the wound healing process through angiogenesis (as discussed in the previous section), which helps in repairing and remodelling the tissue via carrying nutrients and oxygen to the wounded site.

The levels of cytokine markers were checked using ELISA KIT on three different phases of wound healing, i.e.; inflammatory phase (0th day), proliferative phase (7th day) and remodelling phase (14th day). During these phases of wound healing, the inflammatory markers level changes significantly and they manifest the effectiveness of applied nanoformulation. It is observed that on the 14th day of post-treatment, the relative levels of TNF-α, IL-1β and IL-6 are apparently lower than the control and base groups (Figure 9 (a-c)). The C-reactive protein (CRP) is generally released from the liver into the bloodstream due to the reaction of inflammatory cytokines. After any injury or damage, the CRP level suddenly increases, and with time, as the wound heals, the CRP level decreases. Herein, also on the 0th and 14th day of post-treatment, CRP levels are observed to be high in the case of control as compared to the p(NAG-*co*-NAPA)$_{wc}$ nanoformulation group (Figure 9 (d)). On the 7th and 14th day of post-treatment, increased levels of IGF-1 are observed for the p(NAG-*co*-NAPA)$_{wc}$ nanoformulation group, which suggests a higher rate of migration of keratinocytes to the damaged site (Figure 9 (e)).[41] In contrast to the above findings, base is also showing wound healing capacity, and on the 7th day of post-treatment, an increased level of pro-inflammatory (TNF-α, IL-1β and IL-6) markers is observed as compared to the control group. This deterrent effect is observed due to the inflammation generated by base and it is clearly matching with the images obtained on the 7th day of post-treatment (Figure 8 (b8)). Furthermore, to study the relative fold change in selected gene expressions, an RT-PCR study was conducted as mentioned in the method section and is shown in Figure 9 (f) and (g). It can be noted that, here in this study, GAPDH was used as a housekeeping gene, and the control group's normal and wounded tissue's gene expression values are considered as internal control for normal and wounded tissues of base and p(NAG-*co*-NAPA)$_{wc}$ nanoformulation treated groups, respectively. RT-PCR studies of 14th day tissue samples revealed that, in the base group although the expression level of wounded tissue's TNF-α is decreased as compared to the normal tissue, however IL-1β expression level is found to be higher in value. This increased IL-1β expression in

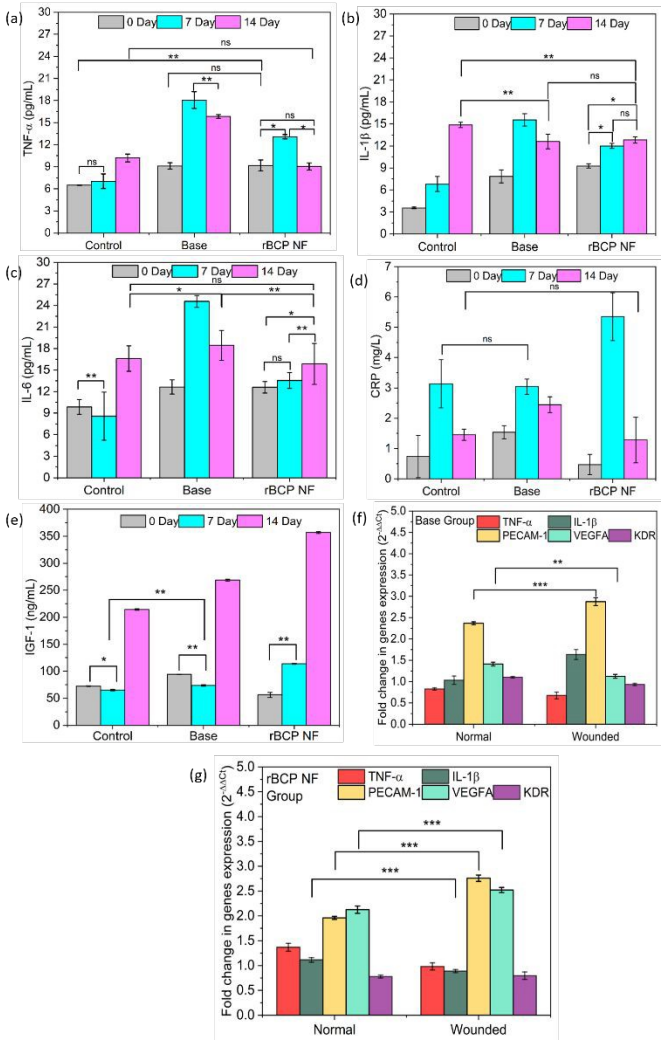

Figure 9. Wound healing markers and real time expressions of selected genes during in vivo wound healing. (a) TNF-α, (b) IL-1β, (c) IL-6, (d) CRP and (e) IGF-1 levels analysed by ELISA on 0th day (before wound creation), 7th and 14th day. Each data point represents the average ±SD of three independent determinations ($p< 0.05$). (f) and (g) Represents relative fold change in gene expressions (TNF-α, IL-1β, PECAM-1, VEGFA and KDR) obtained from RT-PCR results. Other than represented statistical significance, all other combinations are significant with P ≤ 0.001. rBCP NF represents p(NAG-*co*-NAPA)$_{wc}$ nanoparticles based nanoformulation. Data are given as mean ±SD (n=3) (*P ≤ 0.05, **P ≤ 0.05-0.01, ***P ≤ 0.05-0.001 and ns: non-significant).

wounded tissue demonstrates that although ~88% of the wound is covered, still inflammation is present at the wound site. Further, PECAM-1 (CD31) plays a central regulatory role in wound healing and helps in angiogenesis. Compared to normal tissue, in wounded tissue, PECAM-1 expression is highly increased. In the process of wound healing, VEGF-A (Vascular Endothelial Growth Factor A) contributes both directly and indirectly to the migration of inflammatory cells and keratinocytes by stimulating cell proliferation

View Article Online DOI: 10.1039/D5NR00281H

and collagen deposition in the remodelling phase and interacts with the KDR receptor (Kinase Insert Domain Receptor), facilitating its internalization into the nucleus. This interaction ultimately leads to the activation of the PI3-kinase/AKT signalling pathway.[42, 43] Although, for wounded tissues, the expression values of VEGFA and KDR are decreased with respect to the normal group, however these changes are statistically non-significant. Furthermore, in the p(NAG-*co*-NAPA)$_{wc}$ nanoformulation treated groups, for TNF-α and IL-1β, a decrease in gene expression values are observed for wounded tissue as compared to the normal tissue, which signifies that the wound is fully covered with no inflammation. For PECAM-1 and VEGEA an increase in gene expression levels are observed, which is evident from the earlier experiments (Figure 8 (c)). For KDR, no such change in gene expression level is identified. Therefore, it can be suggested that p(NAG-*co*-NAPA)$_{wc}$ nanoformulation possesses an excellent regulatory effect on TNF-α, IL-1β, PECAM-1 and VEGFA genes for wound healing and tissue regeneration.

Discussion

Here, in this work, we have synthesized the physically cross-linker-free amino acid-based p(NAG-*co*-NAPA)$_{wc}$ copolymer nanoparticles with tissue regenerative properties. The synthesis method is based on miniemulsion radical polymerization, which is quite simple and straightforward (Scheme 1). In this synthesis method, we have avoided the use of chemical cross-linkers like DVB or others in order to evade the toxicity generated due to their presence. [10, 12] The well-designed nanosystems have particle sizes in the submicron range, to ensure effective interactions with biochemical and cellular components.[44] From various chemical and physical characterizations, it is confirmed that p(NAG-*co*-NAPA)$_{wc}$ nanoparticles were formed with a size range of c.a. 120-400 nm (Figure 2 (a-b) and (d-e). From the zeta potential measurement, it is observed that the p(NAG-*co*-NAPA)$_{wc}$ nanoparticles are stable as a suspension (Figure 2 (f)). The optical property and secondary structure of p(NAG-*co*-NAPA)$_{wc}$ nanoparticles are investigated using CD spectroscopy, which demonstrates that p(NAG-*co*-NAPA)$_{wc}$ nanoparticles exist in 100% β-turns form (Figure 2 (g)). Further, the distinct separation between positive and negative bands of CD spectra (Figure 2 (g)) depicts the formation of a self-assembled structure in the selected medium.[28]

Further, a detailed MD simulation study has been performed to check the aggregation behaviour of the p(NAG-*co*-NAPA)$_{wc}$ nanoparticles at three different temperatures (298, 310, and 315 K). Compared to all three temperatures, particularly at 310 K (physiological temperature), the aggregation of the dimers is found to be quite high. This aggregation behaviour revealed the higher stability of nanoparticles at body temperature (Figure 3). From MD simulation, it is further revealed that the p(NAG-*co*-NAPA)$_{wc}$ nanoparticles are self-assembled where two different regions exist, i.e., hydrophobic and hydrophilic. The hydrophobic region is made up of phenyl rings present in the NAPA unit, and the hydrophilic region is based on the carboxylic acid group present in the NAG unit. The calculation of the distance between two benzene rings in a hydrophobic region is found to be in the range of 4.2 to 5.4 Å, which further confirms the existence of π-π interactions between the hydrophobic benzene rings (Scheme 2). It is further confirmed that self-assembled porous p(NAG-*co*-NAPA)$_{wc}$ nanoparticles are formed by noncovalent crosslinking and due to the π-π interactions or π stacking. Simultaneously, dynamics of p(NAG-*co*-NAPA)$_{wc}$ nanoparticle has been studied at the POPC bilayer membrane, which is an important aspect for *in vivo* studies (Figure 4 (i) and (j)). These interaction studies revealed the biocompatible nature of p(NAG-*co*-NAPA)$_{wc}$ nanoparticles. It is important to note that, although a concentrated system was employed in simulations to investigate the structure and biocompatibility of the p(NAG-co-NAPA)$_{wc}$ nanoparticles, the results obtained were found to be in good agreement with experimental observations conducted at a diluted concentration (self-assembly behaviour of the nanoparticle (Figure 3) with good colloidal stability (Figure 2 (f)) and close association of dimer unit with POPC bilayer Figure 4 (j) i.e., biocompatible nature of the nanoparticle Figure 5 (a).

Further to establish the biomedical applications of p(NAG-*co*-NAPA)$_{wc}$ nanoparticles, cytocompatibility and hemocompatibility of p(NAG-*co*-NAPA)$_{wc}$ nanoparticles have been checked. It is found that the p(NAG-*co*-NAPA)$_{wc}$ nanoparticles are proliferative in L929 mouse fibroblast cells up to 1000 μg mL^{-1} (Figure 5 (a)). The hemocompatibility study confirmed that the designed NPs are non-hemolytic in rat erythrocytes as compared to +ve control (Figure 5 (b)), which means that the p(NAG-*co*-NAPA)$_{wc}$ nanoparticles do not interfere with the mechanisms of Na+/K+ ATPase and aquaporins.[45] The migration and proliferation of fibroblasts in the presence of biomaterials are essential processes in the healing of skin wounds. The ability of p(NAG-*co*-NAPA)$_{wc}$ nanoparticles to promote both proliferation and migration supports the idea that they aid in re-epithelialization and the restoration of skin functions (Figure 5 (c)).[46] During acute injury, blood vessel damage leads to the nutrient and oxygen shortages in tissues. From *in ovo* CEMA assay, it is found that p(NAG-*co*-NAPA)$_{wc}$ nanoparticles help to enhance the vascular sprouting and angiogenesis, particularly at lower concentrations (Figure 6). These *in vitro* and *in ovo* results confirm that p(NAG-*co*-NAPA)$_{wc}$ nanoparticles can be used in *in vivo* wound healing.

For *in vivo* study, medical grade materials were used to develop p(NAG-*co*-NAPA)$_{wc}$ nanoformulation and underwent standard quality control tests for preclinical studies, ensuring its suitability for topical applications by adjusting for skin pH using triethanolamine (Table S3). Further, homogeneity and spreadability are crucial for any nanoformulation as lack of uniformity can lead to secondary injuries by causing delayed healing processes. Therefore, conducting a dermal irritancy test is essential. After applying the formulation, it is assessed for erythema and edema using the Draize scoring scale (Table S4), with results converted into PDII values via eqn. (3). The p(NAG-*co*-NAPA)$_{wc}$ nanoformulation was applied on rat skin and was compared with the standard irritant, i.e., formalin. Except positive control, no rats showed cutaneous irritation (Figure 7 (b2) and (c2)). Additionally, a period of 7-days observation was carried out for all groups, and none of the animals showed any unusual behaviour. Furthermore, the wound healing capacity of p(NAG-*co*-NAPA)$_{wc}$ nanoformulation was carried out using Wistar rats by generating an 8-10 mm wound on the rats. It is observed that within 13th day of post-treatment, major part of the wound is covered as compared to the base and control group (Figure 8 (b5), (b10) and (b15)). Although the base and p(NAG-*co*-NAPA)$_{wc}$ nanoformulation-treated groups are showing similar extents of wound-covered areas up to the 10th day post-treatment, on the 13th day of treatment, the whole wound was covered for the p(NAG-*co*-NAPA)$_{wc}$ nanoformulation-treated groups. These findings are matching well with the results obtained from the histology study of 14th day old wounds, which demonstrates the formation of dense and dispersed fibroblast cells in the p(NAG-

co-NAPA)$_{wc}$ nanoformulation treated groups as compared to the base and control group (Figure 7 (b18)).[47, 48]

Finally, the study focused on the inflammatory, proliferative and remodelling phases of wound healing, i.e., 0th, 7th and 14th day of treatment, respectively. It is observed that the topically applied p(NAG-*co*-NAPA)$_{wc}$ nanoformulation influenced various chemokines, cytokines and growth factors in the systemic blood of both control and treated groups of animals in all these three days. The p(NAG-*co*-NAPA)$_{wc}$ nanoformulation-treated groups exhibited almost equal levels of TNF-α, IL-1β and IL-6 (Figure 8 (a), (b), and (c)), indicating effective anti-inflammatory regulation by p(NAG-*co*-NAPA)$_{wc}$. For CRP, also a decrease in marker level is observed on the 14th day of post-treatment for the p(NAG-*co*-NAPA)$_{wc}$ nanoformulation-treated groups, which demonstrates that no inflammation persists on the wound site. While for the base, although the wound is relatively closed as compared to the control group, CRP is still higher in value on the 14th day (Figure 9 (d)). By day 14th, IGF-1 levels significantly increased in the treated groups, suggesting enhanced keratinocyte migration towards the wound site (Figure 9 (e)). This rise in IGF-1 values is also correlated with the increased vascularity, as it activates the PI3-kinase/Akt signalling pathway and upregulates PDGFB, MMPs and other angiogenic growth factors.[22] Additionally, the RT-PCR results of the 14th day of tissue samples revealed that comparing to the base group, in p(NAG-*co*-NAPA)$_{wc}$ nanoformulation-treated groups, TNF-α and IL-1β expression levels are lower and VEGFA and PECAM-1 expression levels are higher, which clearly signifies that p(NAG-*co*-NAPA)$_{wc}$ nanoformulation has a strong correlation with regulatory genes related to wound healing and tissue regeneration (Figure 9 (f) and (g)). Hence, from this work it can be stated that this self-assembled physically cross-linked p(NAG-*co*-NAPA)$_{wc}$ can efficiently act as a potential regenerative medicine.

Conclusions

In summary, we have successfully synthesized a novel self-assembled amino acid-based random di-block copolymer nanoparticles of NAG and NAPA, i.e., p(NAG-*co*-NAPA)$_{wc}$. From various spectroscopy studies, it is confirmed that p(NAG-*co*-NAPA)$_{wc}$ was formed via mini-emulsion radical polymerization without using any additional covalent cross-linker. The H-bonds caused by carboxylic acid groups of NAG and π-π stacking caused by the phenyl ring of NAPA triggered non-covalent cross-linking and accelerated the formation of self-assembled spherical p(NAG-*co*-NAPA)$_{wc}$ nanoparticles and promoted the construction of a beautiful network-like structure. MD simulation studies also revealed that the p(NAG-*co*-NAPA)$_{wc}$ nanoparticles formed aggregates in the temperature range of 298 to 315 K. In aggregates, hydrophobic and hydrophilic groups can make separate domains and show interactions in close proximity. As anticipated, the hemolysis study and *in vitro* cytotoxicity assay revealed that p(NAG-*co*-NAPA)$_{wc}$ nanoparticles are hemocompatible and cytocompatible in nature. The exciting hallmarks, angiogenesis, cell migration, and proliferation properties established the regenerative property of p(NAG-co-NAPA) nanoparticles. Additionally, *in vivo* experiments demonstrated p(NAG-*co*-NAPA)$_{wc}$ nanoformulation's potential for its use in regenerative medicine, i.e., acute wound healing without additional growth factors such as cytokines, cells, or genes, etc. Thus, p(NAG-*co*-NAPA)$_{wc}$ nanoparticles are paramount for clinical and therapeutic applications.

Materials and methods

View Article Online
DOI: 10.1039/D5NR00281H

Materials

All the chemicals were used without further purification unless otherwise stated. Glycine (98%, Qualigens), L-Phenylalanine methyl ester (Sigma), Triethylamines (≥99.5%, Merck), 1, 4-dioxane (99%) extra pure (Merck), Potassium Hydroxide (KOH), 2,2'- Azo-bis-isobutyronitrile (AIBN, 98%, SRL), SDS (sodium dodecyl sulfate) (90%, Merck), Magnesium sulphate Anhydrous (SRL), Hexadecane anhydrous (HD) (99%, Sigma –Aldrich), (Alfa Aesar), Acryloyl chloride stab with 400ppm phenothiazine (96%, Alfa aesar), Ethyl acetate, Hydrochloric acid, Diethyl Ether, Anhydrous Dichloromethane, Sodium bisulphate, Sodium Chloride, Toluene, DMSO d6, CDCl3, Phosphate buffered saline (pH 7.4), Isopropanol, Phosphotungestic acid, DNS (Sodium Chloride and Dextrose Injection IP (0.9% & 5% w/v)) (Jedux), Methyl thiazoltetrazolium (MTT, >99.9%, Himedia), Dulbecco's modified Eagle medium (DMEM, Cell Clone), Trypsin-EDTA, 4% Paraformaldehyde solution (Himedia), Fetal Bovine serum (FBS, Gibco), Penicillin streptomycin cocktail (Himedia), DMSO (Merck), L929 (mouse fibroblast cells) was acquired from NCCS-Pune repository, India; Isoflurane (Abbott), Lidocaine (Abbott), White soft paraffin (SRL), Paraffin wax (SRL), Glycerine (SRL), Steryl alcohol (SRL), Liquid paraffin (SRL), Triethanolamine (Loba Chemie, 98%), Hematoxylin (SRL), Eosin (Himedia), Triazole (Invitrogen), Chloroform (Merck) and Diethyl polycarbonate treated water (DEPC-treated water, Himedia). Pure Lab Ultra water system (ELGA, High Wycombe, United Kingdom) was used to obtain Ultrapure water (18.2 M) for sample processing.

Synthesis of NAG and NAPA monomers

The synthesis of monomers, NAG and NAPA, was performed according to our previously reported approach.[3, 23]

Synthesis of p(NAG-*co*-NAPA)$_{wc}$ block copolymer nanoparticles

The synthesis approach of poly[(N-acryloyl Glycine)-*co*-(N-acryloyl-(L-phenylalanine methyl ester)] p(NAG-*co*-NAPA)$_{wc}$ random block copolymers was quite similar to the procedure followed for the synthesis of pNAPA and PNAG with modifications as reported earlier.[3, 23] In brief, the mixture of two monomers (NAG and NAPA) with a 1:1 ratio was taken by maintaining the total weight to 500 mg. Without DVB, keeping all other parameters fixed, the time for probe sonication was increased to 8.30 minutes, and polymerization was performed. Further, the washing with a 1:1 ethanol and water mixture, for 8-10 times, centrifugation (15,000 RPM at 4 °C for 45 minutes), and freeze-drying (48 h) steps were followed to obtain the dried lyophilized white powder. Then the sample was stored in a sealed container for further studies.

Characterization of NAG, NAPA, and p(NAG-*co*-NAPA)$_{wc}$ nanoparticle

The chemical functionalities were confirmed through the FT-IR (Fourier Transform Infrared) Spectroscopy (Nicolet iS5, THERMO Electron Scientific Instruments LLC) using the ATR method and 1H NMR and 13C NMR spectroscopy (500 MHz One Bay NMR Spectrometer, BRUKER BioSpin INTERNATIONAL AG). Chemical shifts are recorded in ppm relative to the signals generated by deuterated solvents (DMSO-d_6 for NAG and $CDCl_3$ for NAPA, p(NAG-*co*-NAPA)$_{wc}$ and analysis was performed using MestReNova 15.0. Matrix-assisted

View Article Online
DOI: 10.1039/D5NR00281H

laser desorption/ionization-time of flight (MALDI-ToF) mass spectra were measured using a Bruker Autoflex instrument, and the method of analysis was RN_900-4500_Da.par. UV-Vis Spectroscopy (Lambda 750 Spectrophotometer, PerkinElmer) studies were performed in the range of λ = 190-400 nm. The crystallinity of the polymers was assessed using High Resolution X-Ray Diffraction (XRD) (Rigaku SmartLab 9kW Powder type (without χcradle)) in 2θ = 10°-90° equipped with Cu Kα X-Ray source with λ = 1.54 Å. Thermal stability and phase transition of polymers were studied through TGA (TGA-50, M/s Shimadzu (Asia Pacific)) from RT to 600°C, @ 10°C/min heating rate with 100 mL/min of N_2 gas flow and DSC (DSC-60 Plus, M/s Shimadzu (Asia Pacific)) was conducted from 25 to 300°C @ 10°C/min heating rate with 100 mL/min of N_2 gas flow.

Colloidal Stability and Morphological Evaluation

The colloidal stability of the p(NAG-*co*-NAPA)$_{wc}$ nanoparticles was studied using Dynamic light scattering and Zeta sizer (Malvern Zeta Sizer) at 25 °C. DLS and Zeta samples were prepared at 500 µg mL^{-1} in MilliQ water, three acquisitions were recorded, and their average hydrodynamic size and zeta potential values were reported. Circular dichroism (CD, Jasco J-1500 CD Spectrometer) measurements were performed in MilliQ at four different dilutions at RT and three different temperatures with fixed concentration. The spectra were collected from 190 to 300 nm with 0.5 nm data pitch and 1.0 nm bandwidth. For FESEM analysis ~0.1 mg of p(NAG-*co*-NAPA)$_{wc}$ nanoparticles was taken in 500 µL of isopropanol and bath sonicated in regular intervals up to 8 h for uniform dispersion. Then a few drops of copolymer samples were drop-casted over the cleaned silicon wafer and dried. Images were acquired using Nova NanoSEM 450 equipped with Team Pegasus Integrated EDS-EBSD with Octane Plus and Hikari Pro. For HRTEM analysis, ~0.1 mg of polymer samples were taken in 500 µL of isopropanol, and two drops of phosphotungstic acid (PTA) were added and bath sonicated in regular intervals upto 8 h for uniform dispersion. Then a few drops of polymer samples were drop-casted over the carbon coated Cu-grid with 200 mesh size and dried under a tungsten bulb. Images and EDAX patterns were acquired using Tecnai G2 20 TWIN (FEI Company of USA (S.E.A.) PTE, LTD) equipped with TEAM EDS SYSTEM with Octane Plus SDD Detector. For AFM, a sample was prepared similar to FESEM and images were acquired using NTEGRA Prima.

CMC Determination

The CMC was determined using 6-methyl coumarin as a hydrophobic dye based on a previously reported method with slight modification.[49, 50] Once the concentration reaches above to CMC, the dye could associate with the hydrophobic domain of p(NAG-*co*-NAPA)$_{wc}$ nanoparticles and emit strong fluorescence. A stock solution of 6 µM was prepared in dry DCM and then 50 µL of the solution was added to each amber color micro centrifuge tube and kept for 30 minutes in the dark for drying. Further, 400 µL of p(NAG-*co*-NAPA)wc nanoparticles in MilliQ water with different concentrations (1000 µg mL^{-1} to 0.488 µg mL^{-1} with 2-fold serial dilutions) was added and stirred in the dark at 25 °C for 20 h. Then, the emission spectra were recorded using a microplate reader (Biotek) with λ = 285 nm excitation and λ = 410 nm emission. Further, from the emission vs intensity plot a tangent was drawn to determine the CMC.

Molecular Dynamics Simulation

Molecular Dynamics simulations study was performed using GROMACS-2020[51] to understand the micro-structure and dynamics of the p(NAG-*co*-NAPA)$_{wc}$ at different conditions. CHARMM36 force field was used to model the bonded and non-bonded interactions between the various atoms of the atomistically modelled copolymers and water molecules using the following equation:

$$\boldsymbol{U_{nb}(r_{ij})} = \sum \frac{q_i q_j}{4\pi\epsilon_0 r_{ij}} + \sum_{i=1}^{N} 4\epsilon_{ij}\left(\left(\frac{\sigma_{ij}}{r_{ij}}\right)^{12} - 2\left(\frac{\sigma_{ij}}{r_{ij}}\right)^{6}\right), \text{.....(1)}$$

where the non-bonded interactions between i^{th} and j^{th} atoms, having partial charges q, well depth ϵ, distance r, and radius in the Lennard-Jones (LJ) 6-12 term used to treat the van der Waals' interaction σ. The bonded interaction energy contributions are bonds, valence angles, dihedral angles, improper dihedral angles, selected Urey–Bradley along with torsional correction map (CMAP) terms which are further expressed as eqn. no. (2):

$$\begin{aligned} \boldsymbol{U_b} = & \sum_{\boldsymbol{bonds}} \boldsymbol{k_b(b-b_0)^2} + \sum_{\boldsymbol{angles}} \boldsymbol{k_\theta(\theta-\theta_0)^2} \\ & + \sum_{\boldsymbol{UB}} \boldsymbol{k_{UB}\left(r_{1-3}-r_{1-3;0}\right)^2} \\ & + \sum_{\boldsymbol{dihed}} \sum_{\boldsymbol{n=1}}^{\boldsymbol{N}} \boldsymbol{k_n\left(1+\cos\left[\!\left[(n\varphi\right]\!\right]-\delta_n\right)\right)} \\ & + \sum_{\boldsymbol{imp}} \boldsymbol{k_\varphi\,(\varphi-\varphi_0)^2 + CMAP} \quad \text{.....(2)} \end{aligned}$$

500 molecules of the co-polymers were randomly placed within the simulation box considering dimensions of 12 nm × 12 nm × 12 nm. The copolymer molecules were solvated with water, modelled as TIP3P[53] and adequate ions were added to attain 0.15 M NaCl concentration and maintain electroneutrality. To obtain a reasonable starting configuration, the energy of the systems was minimized using the steepest descent algorithm with F_{max} <1000 kJ mol^{-1} nm^{-1}. The short-range interactions cut off for electrostatics and van der Waal's forces of interaction was taken as 1.2 nm, and the long-range electrostatics were treated using the particle mesh Ewald (PME) method.[54] Here, similar experimental temperatures (298 K, 310 K and 315 K) and pressure of 1 atm were maintained during simulations. The temperature and pressure were maintained during simulations using the velocity rescale thermostat with a coupling time of 0.1 ps and the Parrinello-Rahman barostat with a coupling time constant of 2 ps, respectively. The equation of motion was integrated using a leap-frog algorithm in which the updated position was calculated using a Verlet algorithm[51, 52] eqn. no. (3) and eqn. no. (4),

$$\boldsymbol{r(t+\delta t) = 2r(t) - r(t-\delta t) + \frac{f(t)}{m}(\delta t)^2 + O(\delta t^4)} \text{...(3)}$$

and the updated velocity was calculated at the half-integer time step;

$$\boldsymbol{v\left(t+\frac{\delta t}{2}\right) = v\left(t-\frac{\delta t}{2}\right) + \frac{f(t)}{m}(\delta t)} \text{ .....(4)}$$

with a timestep δt of 2 fs.

The production runs were performed for 100 ns, and configurations were stored in every 2 ps for further analysis of the structure dynamics. All the analysis were performed in GROMACS 2023.3-Homebrew software.[55] For all the systems, thermodynamic equilibrium has been achieved, and the properties calculated are ensemble-averaged over the last 5-20 ns of the trajectory. During the production run, the variation of different thermodynamic and structural parameters is shown against time, as shown in Figure S14. The properties of interest for describing the copolymer system include radial distribution function (RDF), hydrogen bonding (HB), solvent-accessible surface area (SASA), mean square displacement

View Article Online
DOI: 10.1039/D5NR00281H

(MSD) and number of contact groups. The visual inspection of the simulation results was carried out using VMD 1.9.4.[56] To ensure the reliability of the obtained results and statistical significance, all the simulations were run three times. The topology file for the copolymer system has been provided in Figure S9. The description of the systems is shown in Table S1.

In vitro cell viability study through MTT assay

The cell viability of the p(NAG-co-NAPA)wc nanoparticles was evaluated using healthy cell line L929, which is a mouse fibroblast cell line. Cells were cultured in 10 % of FBS-supplemented DMEM with 100 U of penicillin-streptomycin antibiotic (complete media) and maintained in an incubator at 37 °C with 5% CO_2. 1×10^4 cells/well were cultured in 96 well plate up to 24 h followed by the addition of different concentrations of p(NAG-*co*-NAPA)$_{wc}$ nanoparticles (1000 µg mL^{-1} to 7.9 µg mL^{-1} with 2-fold serial dilution). After 24 h of incubation, samples were removed and 5 µg mL^{-1} of MTT reagent prepared in fresh media was added to each well and incubated for 4 h. Then, MTT reagent was removed and subsequently 100 µL of DMSO was added per well and again incubated for 20 minutes in the dark. Finally, absorbance was recorded at λmax = 570 nm by using a microplate reader (Biotek, SYNERGY H1M). The cell viability (%) was calculated using eqn. no. (5). Data were collected in three distinct biological replicates; each performed on a different day with different cell passages and three repetitions.

$$\text{Cell viability (\%)}=(OD_{(treatment)})/(OD_{(control)}) \times 100 \ldots\ldots\ldots\ldots\ldots\ldots (5)$$

Hemolysis Study

Hemolysis was conducted on RBCs collected from rat's whole blood. In brief, blood samples were collected by rat cardiac puncture, washed/centrifuged (3500 RPM, 5min., RT) and then homogenized to get a uniform suspension of RBCs in sterile DNS (5×10^6 cells µL^{-1}). For the determination of hemolytic effect of polymeric nanoparticles, RBCs were incubated with different concentrations of p(NAG-co- NAPA)wc (500 µg mL^{-1} to 7.8125 µg mL^{-1} with dilution factor 2) for 2 h and 8 h at 37 °C with 100 RPM. Incubation with DNS and distilled water were considered as negative and positive control, respectively. After incubation, at particular intervals, samples were centrifuged at 3500 RPM for 5 minutes at RT, the supernatant was collected and absorbance was recorded at λ_{max} = 540 nm and % hemolysis was estimated using the eqn. no. (6). Experiments were performed with the same rat blood in three distinct tubes for each concentration of p(NAG-*co*-NAPA)$_{wc}$ nanoparticles.

$$\text{Hemolysis (\%)}=(OD_{(treatment)}-OD_{(negative\ control)})/(OD_{(positive\ Control)}-OD_{(negative\ Control)}) \times 100 \ldots\ldots\ldots (6)$$

In vitro Wound scratch assay

The wound scratch assay *in vitro* was performed to check the cell proliferation and migration properties of p(NAG-*co*-NAPA)$_{wc}$ nanoparticles on a two-dimensional scale. This assay was performed with L929 cells. 2×10^5 cells per well of 12 well plates with 800 µL complete media were taken and incubated for 24 h for 70-80% confluency with adhesion. Then, a linear scratch wound was generated for each well by using a 20 µL sterile tip followed by washing with 1X PBS three times. Then, the desired concentration of p(NAG-*co*-NAPA)$_{wc}$ nanoparticles (250 µg mL^{-1} to 62.5 µg mL^{-1}) were added to the wells. Further images were acquired at 0, 24 and 48 h. Closing wound area (%) and closing rate (%) were calculated using Fiji ImageJ Software.

Chicken Embryo Membrane assay (CEMA).

Fertilized chicken eggs were purchased from a trusted and certified vendor (Ramana Hatchery, Varanasi, Uttar Pradesh, India) and incubated in an egg incubator (37 °C, 50-55% RH) up to 4 days before the experiment. On the day of experiment, using a light-shadow approach, the eggs were tested to check whether embryogenesis had occurred or not. Then, 1-2 mL of albumen was removed for the detachment of the developed chick embryo chorioallantoic membrane, and a small window was created on the top of the eggshell. Further different concentrations of p(NAG-*co*-NAPA)$_{wc}$ nanoparticles were prepared in PBS 7.41 (250, 125 and 62.5 µg), and PBS as a control were added and examined upto 24 hrs. The images were captured at different time intervals (0, 2, 4, and 8 h) using a stereo zoom microscope-mounted Magnus camera (Magcam DC Plus 10, Magnus Opto Systems India Pvt. Ltd.) at a resolution of 10 megapixels and analysed using the Angio tool and Fiji ImageJ software.

Development of p(NAG-*co*-NAPA)$_{wc}$ nanoformulation and macroscopic evaluation.

The p(NAG-*co*-NAPA)$_{wc}$ nanoformulation was prepared by disseminating p(NAG-*co*-NAPA)$_{wc}$ nanoparticles (1% w/w) with an oleaginous base to apply smoothly on the wounds. The composition of the oleaginous base was given in Table S2. p(NAG-*co*-NAPA)$_{wc}$ nanoparticles were initially dispersed on the ointment slab, followed by trituration with base by using a long, broad spatula. Glycerine was added last after complete trituration of the ointment with the base. Then, the p(NAG-*co*-NAPA)$_{wc}$ nanoformulation was stored in an open-mouth airtight container at RT. The nanoformulation was further used for macroscopic qualitative assessment. The parameters considered for macroscopic evaluation are given in Table S3.

Biological Evaluation of p(NAG-*co*-NAPA)$_{wc}$ nanoformulation

Ethical Approval

All animal experiments were carried out in accordance with the guidelines of CPCSEA and approved by the Institutional Animal Ethical Committee (IAEC) of IIT (BHU), Varanasi, Uttar Pradesh, India (Regd. no. 2123/GO/Re/S/21/CPCSEA). The animal ethical approval reference No. is IIT(BHU)/IAEC/2023/048 and Patent Application No. (202511043769).

In vivo skin irritation and sensitization

To check any type of irritation and erythematous reactions, p(NAG-*co*-NAPA)$_{wc}$ nanoformulation was applied on the Wistar rat's skin and observed for 48 h. For this study, ~4 cm^2 rat skin was shaved, and p(NAG-*co*-NAPA)$_{wc}$ nanoformulation was applied with formalin (a common irritant) considered as a control. The treated area was wrapped with a bandage and kept for 48 h. After 48 h, bandages were removed, washed with sufficient amounts of water, and visually examined for any kind of irritation and sensitization. Additionally, high-resolution images were captured and compared with images acquired before treatment. Further, examined rats were kept under observation for checking the edema and erythema. To calculate the skin irritation score, Draize scoring system[57-59] (Table

S4) was used with the primary dermal irritation index (PDII) through eqn. no. (7). Further tissue samples were collected for histology.

PDII=PDI/4……..(7)

'0' indicates no irritation, 0.5–1.9 indicates modest discomfort, 2–4.9 indicates mild irritation, and values above 5 indicate severe irritation.

In vivo wound healing.

The treatment efficiency of p(NAG-*co*-NAPA)$_{wc}$ nanoformulation for wound healing was evaluated using Wistar rats. Initially, 3% isoflurane was used to anesthetize the rats, followed by the removal of hairs at the back using a trimmer. Then, lidocaine, a local anaesthetic, was applied at the target site. An 8-10 mm full-thickness cutaneous wound was generated at the shaved site by using a sterile 8 mm biopsy punch. Cleaned the wound region with sterile cotton and topically treated with ~50-60 mg of p(NAG-*co*-NAPA)$_{wc}$ nanoformulation on each alternative day (0th to 12th, once in each alternative day). Wounded regions were covered with a conventional sterile gauze bandage. The dressing was replaced with a fresh bandage after each treatment. Similar steps were followed for the control group for the base as well.

Study of histology and immunochemical assay.

For histology study, on the day 15th of post-treatment, from cicatricial tissue, deep granulation tissue and cross-sectional full-thickness skin specimens were collected. Then, specimens were fixed and embedded in formalin and paraffin wax, respectively. Blocks were further sectioned with a thickness of 5 µm in the transverse plane. The sections were stained with hematoxylin and eosin, then mounted on glass slides and subsequently analysed using an optical microscope at 20x magnification. For immunochemical analysis, the blood serum sample was isolated from rats. The blood samples were collected on three different days (0th, 7th and 14th day), which represented distinct phases of the wound healing cycle and were stored at −80 °C for further processing. Then the level of the Immune markers such as IL-1β, IL-6, CRP, TNF-α and IGF-1 were estimated using commercially available enzyme-linked immunosorbent assay (ELISA) kits as per the instruction. The relative protein concentrations were estimated by recording the absorbance at λ_{max} = 450 nm and compared with the control samples.

Reverse transcription and polymerase chain reaction (RT-PCR).

On the 14th day of post-treatment, nearly 1 mm thickness of tissues was collected from excised wounds and also from the normal skin of all the groups, respectively. RNA was isolated by homogenizing tissue samples in 1 mL of TRIAZOL reagent followed by chloroform extraction. The aqueous layer was collected, and RNAs were precipitated in 1 mL of isopropyl alcohol and centrifuged (12,000g) at 4 °C for 15 minutes. The RNA pellets were washed with 70% ice-cold ethanol for 2 times and suspended in DEPC-treated water. Afterward, RNA was quantified. Then, 1 µg of RNA sample was used for cDNA synthesis using oligo dT sequence and reverse transcriptase polymerase as per the manufacturer's protocol.

RT-PCR (QuantStudio 5, Applied Biosystems) was setup using diluted cDNA samples (1:100) in a final volume of 20 µL using PowerUpTM SYBRTM GREEN Master Mix (Invitrogen) and different optimized concentrations of KiCqStart® primers (sigma) for biomarker target genes such as KDR(5'-AAACTGGATAAAATGGGCG-3') and (3'-AGCCTTTTA GGTAGAGTCAG-5'), VEGFA(5'-CTCATCTCTCCTATGTGCTG -3') and (3'-GATAGAGTATATCTTCAAGCCG-5'), PECAM-1 (5'-AAAACCACAATTGAGTACCAG-3') and (3'-ACTTAGCTTGACGTTCTTTG-5'), IL-1β (5'-GGATGATGATGATAACCTGC-3') and (3'-CATGGAGAATATCACTTGTTGG-5'), TNF-α (5'-CTATGTCTCAGCCTCTTCTC-3') and (3'- CATTTGCCAACTTGCCATCC-5') and GAPDH (5'-TCGGAGTCAACGGATTTG-3') and (3'-GAGACCATTTCACCTATAACAAC-5') as housekeeping gene using Taq polymerase (TAKARA R001A) with 40 repetitive cycles of denaturation at 95 °C for 25 s, annealing for 30 s at 60 °C, extension at 72 °C for 35 s and final extension for 7 minutes at 72 °C. RT-PCR experiments were performed in triplicate for all the samples along with control. The fold change in selected gene expressions with respect to the control was calculated using the comparative Ct method.[58]

Statistical Significance.

One-way ANOVA with Turkey test and independent Student's t-test were used to statistically evaluate the *in vitro* and *in vivo* data using Origin software (OriginLab Corporation, Northampton, USA). The statistical significance in comparison groups was calculated by considering $p<0.05$. The data are represented as a mean of ±SD or unless otherwise stated.

Author contributions

P.P. and D.B. are the principal investigator (PI) of this project. Ideation, experimental designs, result analysis, and manuscript writing are mainly carried out by S.P., P.P., and D.B. D.D.Y. helped in MD simulation, and *in vivo* study was helped by G.S., P.S.S., and A.S.K. RT-PCR study was helped by Jyotirmayee. D.P. helped in the *in vivo* irritation study, and A.R.M. helped in designing the schemes. Manuscript written and finalized by S.P., D.B., and P.P. All the authors have checked the manuscript and approved for the submission.

Conflicts of interest

The authors declare no competing financial interest.

Data availability

The data supporting this study are available in the ESI of this article.

Acknowledgements

The authors acknowledge financial support awarded to Prof. Paik by I-DAPT (File no. I-DAPT/IT (BHU)/2023-24/ Project Sanction/47), Indian Council of Medical Research (ICMR), India (Ref: EMDR/SG/12/2023-4724), STARS-IISc Bangalore (Ref. MoE-STARS/STARS-2/2023-0318), and Anusandhan National Research Foundation, India (Ref: CRG/2023/005576). Sukanya acknowledges the DST-INSPIRE fellowship (IF180185) awarded and financial support from ICMR to carry out the Ph.D. work. Authors also acknowledge the Start-up company: Triphan Healthcare Pvt. Ltd., at I3F, IIT(BHU), Varanasi, India, for the instrumental support. The authors acknowledge Dr. Monika Singh for giving

View Article Online
DOI: 10.1039/D5NR00281H

access to Biorender to draw ToC, Dr. Avanish Singh Parmar (Department of Physics, IIT (BHU)) for the Zeta Analyser and Dr. Alakh Niranjan Sahu (Department of Pharmaceutical Engineering and Technology, IIT (BHU)) for the UV-Vis spectroscopy facility. The ParamShivay Supercomputing Facility at IIT (BHU), Varanasi, funded by MeitY under the National Supercomputing Mission, was used to conduct the MD simulations.

View Article Online
DOI: 10.1039/D5NR00281H

Full Research Paper

References

1. O. J. Deane, J. Jennings and S. P. Armes, *Chemical Science*, 2021, **12**, 13719-13729.
2. H. Sun, D. Liu and J. Du, *Chemical Science*, 2019, **10**, 657-664.
3. A. K. Yamala, V. Nadella, Y. Mastai, H. Prakash and P. Paik, *Nanoscale*, 2017, **9**, 14006-14014.
4. A. K. Yamala, V. Nadella, Y. Mastai, H. Prakash and P. Paik, *Journal of Applied Polymer Science*, 2020, **137**, 48363.
5. Y. Que, Y. Liu, W. Tan, C. Feng, P. Shi, Y. Li and H. Xiaoyu, *ACS Macro Letters*, 2016, **5**, 168-173.
6. X. Liu, Q. Su, J. Zhu and X. Song, *Polymers*, 2023, **15**, 2490.
7. M. Talelli, M. Barz, C. J. F. Rijcken, F. Kiessling, W. E. Hennink and T. Lammers, *Nano Today*, 2015, **10**, 93-117.
8. C. Deng, Y. Jiang, R. Cheng, F. Meng and Z. Zhong, *Nano Today*, 2012, **7**, 467-480.
9. C. H. Jeong, D. H. Kim, J. H. Yune, H. C. Kwon, D.-M. Shin, H. Sohn, K. H. Lee, B. Choi, E. S. Kim, J. H. Kang, E. K. Kim and S. G. Han, *Toxicology in Vitro*, 2021, **70**, 105034.
10. M. Hanson and A. Wypych, in *Databook of Curatives and Crosslinkers*, eds. M. Hanson and A. Wypych, ChemTec Publishing, 2019, DOI: https://doi.org/10.1016/B978-1-927885-49-9.50003-7, pp. 1-2.
11. J. Chen, E. S. Garcia and S. C. Zimmerman, *Accounts of Chemical Research*, 2020, **53**, 1244-1256.
12. C. Amgoth, G. Dharmapuri, S. Patra, K. Wasnik, P. Gupta, A. M. Kalle and P. Paik, *Journal of Applied Polymer Science*, 2021, **138**, 50386.
13. Y. Shao, W. Huang, C. Shi, S. T. Atkinson and J. Luo, *Therapeutic Delivery*, 2012, **3**, 1409-1427.
14. S. Buwalda, A. Al Samad, A. El Jundi, A. Bethry, Y. Bakkour, J. Coudane and B. Nottelet, *Journal of Colloid and Interface Science*, 2018, **514**, 468-478.
15. Q. Hu, C. J. F. Rijcken, E. van Gaal, P. Brundel, H. Kostkova, T. Etrych, B. Weber, M. Barz, F. Kiessling, J. Prakash, G. Storm, W. E. Hennink and T. Lammers, *Journal of Controlled Release*, 2016, **244**, 314-325.
16. M. Lin, Y. Dai, F. Xia and X. Zhang, *Materials Science and Engineering: C*, 2021, **119**, 111626.
17. J. Chen, B. Yan, X. Wang, Q. Huang, T. Thundat and H. Zeng, *Polymer Chemistry*, 2017, **8**, 3066-3073.
18. G. Wu, C. Li, X. Liu, J. Lv, Y. Ding, Y. Liu, Y. Liu, F. Huang, L. Shi, Y. An and R. Ma, *Colloids and Surfaces B: Biointerfaces*, 2019, **180**, 376-383.
19. W.-R. Zhuang, Y. Wang, P.-F. Cui, L. Xing, J. Lee, D. Kim, H.-L. Jiang and Y.-K. Oh, *Journal of Controlled Release*, 2019, **294**, 311-326.
20. H. Hosseinkhani, P.-D. Hong and D.-S. Yu, *Chemical Reviews*, 2013, **113**, 4837-4861.
21. D. W. P. M. Löwik and J. C. M. van Hest, *Chemical Society Reviews*, 2004, **33**, 234-245.
22. P. S. Gupta, K. Wasnik, S. Patra, D. Pareek, G. Singh, D. D. Yadav, S. Maity and P. Paik, *Nanoscale*, 2024, **16**, 1770-1791.
23. P. S. Gupta, K. Wasnik, G. Singh, S. Patra, D. Pareek, D. D. Yadav, M. S. Tomar, S. Maiti, M. Singh and P. Paik, *Materials Advances*, 2023, **4**, 4718-4731.
24. C. A. Hunter and J. K. M. Sanders, *Journal of the American Chemical Society*, 1990, **112**, 5525-5534.
25. J. Jiang, O. V. Lima, Y. Pei, Z. Jiang, Z. Chen, C. Yu, J. Wang, X. C. Zeng, E. Forsythe and L. Tan, *ACS Nano*, 2010, **4**, 3773-3780.
26. H. S. Purohit, N. S. Trasi, D. D. Sun, E. C. Y. Chow, H. Wen, X. Zhang, Y. Gao and L. S. Taylor, *Journal of Pharmaceutical Sciences*, 2018, **107**, 1330-1341.
27. A. Schittny, J. Huwyler and M. Puchkov, *Drug Delivery*, 2020, **27**, 110-127.
28. L. Werber, L. C. Preiss, K. Landfester, R. Muñoz-Espí and Y. Mastai, *Chirality*, 2015, **27**, 613-618.
29. N. Amdursky and M. M. Stevens, *ChemPhysChem*, 2015, **16**, 2768-2774.
30. L. Adler-Abramovich, L. Vaks, O. Carny, D. Trudler, A. Magno, A. Caflisch, D. Frenkel and E. Gazit, *Nature Chemical Biology*, 2012, **8**, 701-706.
31. Y. Lu, E. Zhang, J. Yang and Z. Cao, *Nano Research*, 2018, **11**, 4985-4998.
32. S. Kim, Y. Shi, J. Y. Kim, K. Park and J.-X. Cheng, *Expert Opinion on Drug Delivery*, 2010, **7**, 49-62.
33. E. Rideau, R. Dimova, P. Schwille, F. R. Wurm and K. Landfester, *Chemical Society Reviews*, 2018, **47**, 8572-8610.
34. S. Yorulmaz Avsar, M. Kyropoulou, S. Di Leone, C.-A. Schoenenberger, W. P. Meier and C. G. Palivan, *Frontiers in Chemistry*, 2019, **6**.

35. Y. Zhao, J. Li, H. Gu, D. Wei, Y.-c. Xu, W. Fu and Z. Yu, *Interdisciplinary Sciences: Computational Life Sciences*, 2015, **7**, 211-220.

36. O. Maksimenko, J. Malinovskaya, E. Shipulo, N. Osipova, V. Razzhivina, D. Arantseva, O. Yarovaya, U. Mostovaya, A. Khalansky, V. Fedoseeva, A. Alekseeva, L. Vanchugova, M. Gorshkova, E. Kovalenko, V. Balabanyan, P. Melnikov, V. Baklaushev, V. Chekhonin, J. Kreuter and S. Gelperina, *International Journal of Pharmaceutics*, 2019, **572**, 118733.

37. S. Cometa, C. Licini, M. A. Bonifacio, P. Mastrorilli, M. Mattioli-Belmonte and E. De Giglio, *Carbohydrate Polymers*, 2022, **283**, 119145.

38. E. Zudaire, L. Gambardella, C. Kurcz and S. Vermeren, *PLOS ONE*, 2011, **6**, e27385.

39. R. Li, K. Liu, X. Huang, D. Li, J. Ding, B. Liu and X. Chen, *Advanced Science*, 2022, **9**, 2105152.

40. G. S. Schultz, G. A. Chin, L. Moldawer and R. F. Diegelmann, *Mechanisms of vascular disease: A reference book for vascular specialists [Internet]*, 2011.

41. P. Deng, L. Yao, J. Chen, Z. Tang and J. Zhou, *Carbohydrate Polymers*, 2022, **276**, 118718.

42. T. A. Wilgus, *Advances in Wound Care*, 2018, **8**, 671-678.

43. I. Domingues, J. Rino, J. A. A. Demmers, P. de Lanerolle and S. C. R. Santos, *PLOS ONE*, 2011, **6**, e25668.

44. M. Moreno-Sastre, M. Pastor, A. Esquisabel, E. Sans, M. Viñas, D. Bachiller and J. L. Pedraz, *Journal of Microencapsulation*, 2016, **33**, 636-645.

45. I. Greco, N. Molchanova, E. Holmedal, H. Jenssen, B. D. Hummel, J. L. Watts, J. Håkansson, P. R. Hansen and J. Svenson, *Scientific Reports*, 2020, **10**, 13206.

46. G. Han, L. N. Nguyen, C. Macherla, Y. Chi, J. M. Friedman, J. D. Nosanchuk and L. R. Martinez, *The American Journal of Pathology*, 2012, **180**, 1465-1473.

47. H. Rostami, R. Mohammadi, S. Asri-Rezaei and A. A. Tehrani, *Iranian Journal of Veterinary Surgery*, 2018, **13**, 14-22.

48. T. Kardan, R. Mohammadi, S. Taghavifar, M. Cheraghi, A. Yahoo and K. Mohammadnejad, *The International Journal of Lower Extremity Wounds*, 2021, **20**, 263-271.

49. H. Su, F. Wang, W. Ran, W. Zhang, W. Dai, H. Wang, C. F. Anderson, Z. Wang, C. Zheng, P. Zhang, Y. Li and H. Cui, *Proceedings of the National Academy of Sciences*, 2020, **117**, 4518-4526.

50. A. Fluksman and O. Benny, *Analytical Methods*, 2019, **11**, 3810-3818.

51. H. Bekker, H. Berendsen, E. J. Dijkstra, S. Achterop, R. Drunen, D. van der Spoel, A. Sijbers, H. Keegstra, B. Reitsma and M. K. R. Renardus, *Physics Computing*, 1993, **92**, 252-256.

52. A. Croitoru, S.-J. Park, A. Kumar, J. Lee, W. Im, A. D. MacKerell, Jr. and A. Aleksandrov, *Journal of Chemical Theory and Computation*, 2021, **17**, 3554-3570.

53. P. Mark and L. Nilsson, *The Journal of Physical Chemistry A*, 2001, **105**, 9954-9960.

54. T. Darden, D. York and L. Pedersen, *The Journal of Chemical Physics*, 1993, **98**, 10089-10092.

55. Homebrew Formulae, https://formulae.brew.sh/formula/gromacs, (accessed 24-07-2024, 2024).

56. W. Humphrey, A. Dalke and K. Schulten, *J Mol Graph*, 1996, **14**, 33-38, 27-38.

57. Z. Djerrou, H. Djaalab, F. Riachi, M. Serakta, A. Chettou, Z. Maameri, B. Boutobza and Y. Hamdi-Pacha, *African Journal of Traditional, Complementary and Alternative Medicines*, 2013, **10**, 480-489.

58. M. S. Latif, A. Nawaz, S. A. Rashid, M. Akhlaq, A. Iqbal, M. J. Khan, M. S. Khan, V. Lim and M. Alfatama, *Polymers*, 2022, **14**, 2211.

59. M. W. Pfaffl, *Nucleic Acids Research*, 2001, **29**, e45-e45.

View Article Online
DOI: 10.1039/D5NR00281H

Full Research Paper

View Article Online
DOI: 10.1039/D5NR00281H

Prof. Pradip Paik, ***B.Tech. (C.U) , M.Tech. & Ph.D. (IIT-K)***
NASI (Life Member), TSA (Asso. Fellow)
School of Bio-Medical Engineering

Varanasi, U.P., 221 005, India
Phone.: 08500109932(m)
Fax: +91-..-_____
Email:paik.bme@iitbhu.ac.in,
pradip.paik@gmail.com

Ref:

Date: 9th Jan, 2025

To,
The Editor-in-Chief and Reviewers
Materials Horizon

Sub: **Data Availability Statement**

Manuscript ID: MH-COM-01-2025-000015

Dear Honorable Editor-In-Chief,

"The datasets generated during experiments, computational studies and/or analysis for this article are available from the authors/communicating authors on reasonable request".

Thanking you.
Sincerely Yours,

(Prof. Pradip Paik), On behalf of all the authors